

See discussions, stats, and author profiles for this publication at: <https://www.researchgate.net/publication/335703737>

Numerical study of the stress singularity in stick-slip flow of the Phan-Thien Tanner and Giesekus fluids

Article in Physics of Fluids · September 2019

DOI: 10.1063/1.5100730

CITATIONS

5

READS

76

4 authors:



C.M. Oishi

São Paulo State University

56 PUBLICATIONS 430 CITATIONS

[SEE PROFILE](#)



Jonathan Evans

University of Bath

9 PUBLICATIONS 56 CITATIONS

[SEE PROFILE](#)



Irineu L. Palhares Junior

University of São Paulo

5 PUBLICATIONS 21 CITATIONS

[SEE PROFILE](#)



Jose Alberto Cuminato

University of São Paulo

98 PUBLICATIONS 1,451 CITATIONS

[SEE PROFILE](#)

Some of the authors of this publication are also working on these related projects:



Free surface flows simulations [View project](#)



Asymptotics and Simulation of Complex Fluids [View project](#)

Numerical study of the stress singularity in stick-slip flow of the Phan-Thien Tanner and Giesekus fluids

Cite as: Phys. Fluids **31**, 093101 (2019); <https://doi.org/10.1063/1.5100730>

Submitted: 20 April 2019 . Accepted: 20 August 2019 . Published Online: 09 September 2019

J. D. Evans, J. A. Cuminato , I. L. Palhares Junior , and C. M. Oishi 



[View Online](#)



[Export Citation](#)



[CrossMark](#)

SciLight

Highlights of the best new research
in the physical sciences

AIP
Publishing

[LEARN MORE!](#)

Numerical study of the stress singularity in stick-slip flow of the Phan-Thien Tanner and Giesekus fluids

Cite as: Phys. Fluids 31, 093101 (2019); doi: 10.1063/1.5100730

Submitted: 20 April 2019 • Accepted: 20 August 2019 •

Published Online: 9 September 2019



J. D. Evans,^{1,a)} J. A. Cuminato,² I. L. Palhares Junior,^{2,b)} and C. M. Oishi^{3,c)}

AFFILIATIONS

¹ Department of Mathematical Sciences, University of Bath, Bath, BA2 7AY, United Kingdom

² Departamento de Matemática Aplicada e Estatística Instituto de Ciências Matemática e Computação, Universidade de São Paulo, 13566-590 São Carlos, SP, Brazil

³ Departamento de Matemática e Computação, Faculdade de Ciências e Tecnologia, Universidade Estadual Paulista “Júlio de Mesquita Filho,” 19060-900 Presidente Prudente, SP, Brazil

Note: Papers from the Institute of Non-Newtonian Fluid Mechanics Meeting, Lake Vyrnwy, 2019.

^{a)}E-mail: masjde@bath.ac.uk

^{b)}E-mail: irineulopespalhares@gmail.com Tel.: +55 18 981793481.

^{c)}E-mail: cassio.oishi@unesp.br. Tel.: +55 18 32295623.

ABSTRACT

Stick-slip flow is a challenging viscoelastic benchmark problem due to the presence of a separation or transition point at the die exit where a sudden change in flow boundary conditions occurs. We present numerical simulations of transient planar stick-slip flow of the Phan-Thien-Tanner (PTT) and Giesekus fluids, investigating the polymer stress behavior around the stress singularity at the stick-slip point, confirming the asymptotic results presented by Evans *et al.* [“Stresses of the Oldroyd-B, PTT and Giesekus fluids in a Newtonian velocity field near the stick-slip singularity,” Phys. Fluids **29**, 1–33 (2017)]. In order to improve the numerical knowledge about this viscoelastic benchmark problem, two distinct mathematical methodologies are used for comparison in the computational simulations: the Cartesian and natural stress formulations. The former is widely applied in computational rheology, while the latter is used for the first time in the context of this problem. The natural stress formulation gives improved convergence results both temporally and spatially near to the singularity while maintaining the same global flow characteristics as the Cartesian.

Published under license by AIP Publishing. <https://doi.org/10.1063/1.5100730>

I. INTRODUCTION

A common industrial processing situation involves the extrusion of molten polymers through a die. The dies tend to be rectangular (slit) or capillary (cylindrical), and the polymer is usually melted and pumped through fixed channels and orifices to provide a steady stream of a given cross-sectional profile.¹ It is a process that has received much experimental and theoretical attention due to the following features:

1. Die swell: on leaving the channel, the extrudate can expand (i.e., swell) significantly when viscoelastic materials are involved instead of Newtonian.²

2. Stress singularity: on leaving the die, there is an abrupt change in boundary conditions from one involving velocity on the die wall to that of a stress free surface condition outside the die.^{2–7}
3. Extrudate distortions and fracture: various morphological distortions in the extrudate surface can occur when the wall shear stress exceeds critical values. The surface can change from being smooth to exhibiting sharkskin, spurt (sometimes referred to as stick-slip in reference to changing no-slip and slip wall velocity conditions), and fracture. These instabilities have attracted a lot of attention, see, for example, Petrie and Denn,⁸ Denn,^{9,10} Larson,¹¹ Graham,¹² and more recently, Kwon.¹³

Our focus here is on the situation in which the extrudate's free surface remains smooth and does not deform. This is a particular case of die swell, which is also often referred to as stick-slip flow (in reference to the change in boundary conditions inside the die to the outside). It allows investigation of the singular stress behavior at the die exit, before proceeding to more complex and involved situations. Stick-slip is one of the five benchmark problems¹⁴ proposed for the testing and comparison of numerical techniques.

Real polymeric fluids exhibit properties in simple shear flows such as shear thinning and nonzero normal stress differences.^{2,15} Models, such as Phan-Thien-Tanner (PTT)^{16,17} and Giesekus,¹⁸ capture such effects well and correct deficiencies of simpler models, such as Oldroyd-B,^{2,19} which possesses infinite stresses at finite elongational rates. This is particularly relevant for stick-slip, as elongational flow dominates after emergence of the polymeric fluid from the die. It is also worth remarking that the PTT and Giesekus models are not only applicable to polymer processing of plastics, elastomers, suspensions, and certain food products²⁰ but also to other problems in rheology, such as non-Newtonian hemodynamics,^{21,22} the extrusion process,^{23,24} double-layer optical fibers,²⁵ fluid damper problems,²⁶ and microfluidic flows,^{27,28} to name only a few.

In previous work,²⁹ we categorized the stress singularity for PTT and Giesekus fluids in planar stick-slip flow. Here, we continue the investigation by presenting a numerical scheme for solving the full flow equations. Two distinct formulations of the constitutive equations are presented: one being the traditional Cartesian stress formulation (CSF) using a fixed Cartesian stress basis, while the other is the natural stress formulation (NSF) which aligns the stress along streamlines. We use the schemes to verify the asymptotic results (Refs. 30, 31, and 29) at the singularity for the stress and velocity, as well as the boundary layer structures at the wall (no-slip) and free (slip) surfaces. As for the re-entrant corner singularity,^{32–34} we show that the NSF can more accurately capture the behavior near to the singularity than the CSF. This is also expected to be the case for die swell, where the free-surface is now able to deform.

There is only limited numerical work in the literature for the stick-slip flow of the PTT fluid and apparently no investigation for Giesekus. PTT has been considered by Fortin *et al.*,³⁵ Baaijens,³⁶ Xue *et al.*,³⁷ and Karapetsas and Tsamopoulos.³⁸ Fortin *et al.*³⁵ used a finite element method (FEM) and presented results for the polymer normal stress in the direction of flow and in the absence of a solvent viscosity. Convergence is obtained up to a limiting Weissenberg number Wi_{crit} , which increased as the PTT model parameter ϵ increased ($Wi_{crit} = 2, 13$, and unlimited for $\epsilon = 0, 0.02, 0.25$, respectively). They stated that similar results are obtained with a solvent viscosity, although provided no quantitative details. Baaijens³⁶ used a discontinuous Galerkin FEM to solve the PTT model, again with no solvent viscosity, presenting results up to Deborah number $De = 87$ for a large PTT model parameter $\epsilon = 0.25$ and which reduce to $De = 25.5$ for the upper convected Maxwell (UCM) case of $\epsilon = 0$. Karapetsas and Tsamopoulos³⁸ gave a FEM based on a modified elastic-viscous split stress EVSS-G scheme, which they applied in both planar and cylindrical cases and to the linear and exponential forms of the PTT model. Estimates of the elastic stress singularity are given, although these are almost exclusively for the no solvent viscosity case. There is a solitary result for a solvent viscosity fraction $\beta = 1/9$ for the exponential PTT model. However, in all the

cases where they have numerical results, theoretical knowledge of the singularity is currently unknown. It is only for the linear PTT model with solvent viscosity that the singularity has so far been classified. Our results here then extend the literature by considering this case, as well as presenting the analogous results for the Giesekus model. Moreover, we present a transient scheme, which should be contrasted to all previous schemes which deal only with the steady situation.

The layout of the paper is as follows: The CSF and NSF of the PTT and Giesekus equations are presented in Sec. II including the flow geometry, the mesh description, and the overview of the numerical methods. In Sec. III, we present the numerical convergence results for both formulations, including temporal convergence studies and profile analyses. The stress singularity investigation is conducted in Sec. IV. Not only are the stress singularities numerically verified but also the theoretical boundary layer structures at both the stick and slip surfaces. Although the known theoretical asymptotic results at the singularity are technically valid as long as a solvent viscosity is present in the models, capturing the singularity numerically becomes extremely challenging as the solvent viscosity reduces. Results for $\beta = 1/9$, illustrating this are presented in Sec. IV C. Finally, the influence of Weissenberg number is investigated in Sec. IV D.

II. FLOW EQUATIONS

The geometry and governing equations relevant to this flow are described in Ref. 29. The flow is incompressible with the extra-stress tensor being rheologically decomposed into solvent and polymer components while the geometry used in all simulations is illustrated in Fig. 1. The channel half-width H and mean speed V of the incoming flow are used as characteristic length and velocity scalings, while the pressure and both the solvent and polymer extra-stresses are all scaled using the total viscosity η (comprising solvent η_s and polymer η_p). We remark that this is an alternative nondimensionalization for the extra stresses to that presented in Ref. 29 which used the respective solvent and polymer viscosities instead of the total viscosity. The dimensionless form of the flow equations is

$$\nabla \cdot \mathbf{v} = 0, \quad (2.1)$$

$$Re \left(\frac{\partial \mathbf{v}}{\partial t} + \mathbf{v} \cdot \nabla \mathbf{v} \right) = -\nabla p + \beta \nabla^2 \mathbf{v} + \nabla \cdot \mathbf{T}, \quad (2.2)$$

$$\mathbf{T} + Wi \left(\mathbf{T} + \frac{\kappa}{(1-\beta)} \mathbf{g}(\mathbf{T}) \right) = 2(1-\beta) \mathbf{D}, \quad (2.3)$$

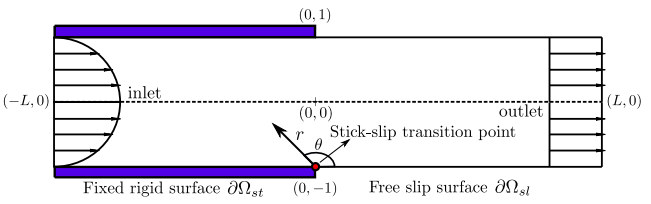


FIG. 1. The stick-slip geometry description. The $(0, -1)$ point represents the stick-slip transition point. The dimensionless domain half-length L is typically taken as 8.

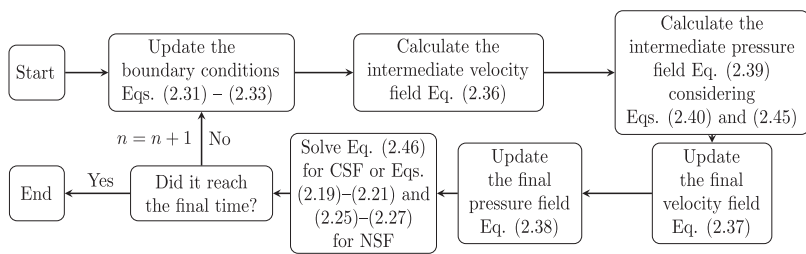


FIG. 2. Flowchart of the numerical schemes.

$$\mathbf{g}(\mathbf{T}) = \begin{cases} \text{tr}(\mathbf{T})\mathbf{T}, & \text{PTT,} \\ \mathbf{T}^2, & \text{Giesekus,} \end{cases} \quad (2.4)$$

with $\mathbf{D} = \frac{1}{2}(\nabla \mathbf{v} + (\nabla \mathbf{v})^T)$ the rate-of-strain tensor and the upper-convected stress derivative defined as

$$\bar{\mathbf{T}} = \frac{\partial \mathbf{T}}{\partial t} + (\mathbf{v} \cdot \nabla) \mathbf{T} - (\nabla \mathbf{v}) \mathbf{T} - \mathbf{T} (\nabla \mathbf{v})^T. \quad (2.5)$$

The dimensionless parameters are the Reynolds number Re , Weissenberg number Wi , and retardation parameter $\beta \in [0, 1]$ (the dimensionless retardation time or dimensionless solvent viscosity). The model parameter κ is the coefficient of the quadratic stress terms representing the PTT model parameter (ϵ being commonly used) or Giesekus mobility factor.

In component form relative to fixed Cartesian axes, Eqs. (2.1)–(2.3) can be rewritten as

$$\frac{\partial u}{\partial x} + \frac{\partial v}{\partial y} = 0, \quad (2.6)$$

$$\text{Re} \left(\frac{\partial u}{\partial t} + u \frac{\partial u}{\partial x} + v \frac{\partial u}{\partial y} \right) = -\frac{\partial p}{\partial x} + \beta \left(\frac{\partial^2 u}{\partial x^2} + \frac{\partial^2 u}{\partial y^2} \right) + \frac{\partial T_{11}}{\partial x} + \frac{\partial T_{12}}{\partial y}, \quad (2.7)$$

$$\text{Re} \left(\frac{\partial v}{\partial t} + u \frac{\partial v}{\partial x} + v \frac{\partial v}{\partial y} \right) = -\frac{\partial p}{\partial y} + \beta \left(\frac{\partial^2 v}{\partial x^2} + \frac{\partial^2 v}{\partial y^2} \right) + \frac{\partial T_{12}}{\partial x} + \frac{\partial T_{22}}{\partial y}, \quad (2.8)$$

$$T_{11} + \text{Wi} \left(\frac{\partial T_{11}}{\partial t} + u \frac{\partial T_{11}}{\partial x} + v \frac{\partial T_{11}}{\partial y} - 2 \frac{\partial u}{\partial x} T_{11} - 2 \frac{\partial u}{\partial y} T_{12} + \frac{\kappa}{(1-\beta)} g_{11} \right) = 2(1-\beta) \frac{\partial u}{\partial x}, \quad (2.9)$$

$$T_{22} + \text{Wi} \left(\frac{\partial T_{22}}{\partial t} + u \frac{\partial T_{22}}{\partial x} + v \frac{\partial T_{22}}{\partial y} - 2 \frac{\partial v}{\partial y} T_{22} - 2 \frac{\partial v}{\partial x} T_{12} + \frac{\kappa}{(1-\beta)} g_{22} \right) = 2(1-\beta) \frac{\partial v}{\partial y}, \quad (2.10)$$

$$T_{12} + \text{Wi} \left(\frac{\partial T_{12}}{\partial t} + u \frac{\partial T_{12}}{\partial x} + v \frac{\partial T_{12}}{\partial y} - \frac{\partial v}{\partial x} T_{11} - \frac{\partial u}{\partial y} T_{22} + \frac{\kappa}{(1-\beta)} g_{12} \right) = (1-\beta) \left(\frac{\partial u}{\partial y} + \frac{\partial v}{\partial x} \right), \quad (2.11)$$

where Eq. (2.4) is now defined as

$$g_{11} = \begin{cases} (T_{11} + T_{22}) T_{11}, & \text{PTT,} \\ (T_{11}^2 + T_{12}^2), & \text{Giesekus,} \end{cases} \quad (2.12)$$

$$g_{12} = (T_{11} + T_{22}) T_{12}, \quad (2.13)$$

$$g_{22} = \begin{cases} (T_{11} + T_{22}) T_{22}, & \text{PTT,} \\ (T_{12}^2 + T_{22}^2), & \text{Giesekus.} \end{cases} \quad (2.14)$$

We refer to (2.9)–(2.11) as the Cartesian stress formulation of the constitutive equation. An alternative is to align the polymer stress basis along streamlines, thus introducing natural stress variables. We follow closely here the construction of Renardy³² (see also Refs. 39 and 40). Introducing the configuration tensor \mathbf{A} by

TABLE I. Meshes used in the present work.

Mesh	Δx_{min}	Δy_{min}
M1	5.0×10^{-3}	5.0×10^{-3}
M2	5.0×10^{-4}	5.0×10^{-4}
M3	5.0×10^{-5}	5.0×10^{-5}

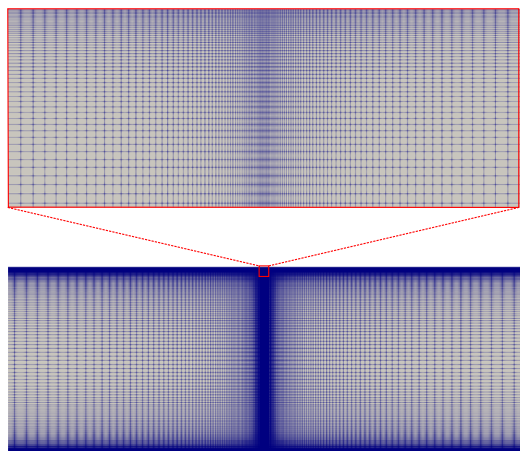


FIG. 3. Visualization details of the nonuniform mesh for the stick-slip problem.

$$\mathbf{T} = \frac{(1-\beta)}{\text{Wi}} (\mathbf{A} - \mathbf{I}), \quad (2.15)$$

the polymer constitutive equation (2.3) becomes

$$\text{Wi} \nabla \cdot \mathbf{A} + (\mathbf{A} - \mathbf{I}) + \kappa \mathbf{g}(\mathbf{A} - \mathbf{I}) = 0, \quad (2.16)$$

after using $\nabla \cdot \mathbf{I} = -2\mathbf{D}$. We now express \mathbf{A} in terms of the dyadic products of \mathbf{v} and an orthogonal vector \mathbf{w} as follows:

$$\mathbf{A} = \lambda \mathbf{v} \mathbf{v}^T + \mu (\mathbf{v} \mathbf{w}^T + \mathbf{w} \mathbf{v}^T) + \nu \mathbf{w} \mathbf{w}^T, \quad (2.17)$$

where

$$\mathbf{v} = (u, v)^T, \quad \mathbf{w} = \frac{1}{|\mathbf{v}|^2} (-v, u)^T,$$

with \mathbf{w} chosen such that $|\mathbf{v} \times \mathbf{w}| = 1$. Computationally, it is convenient to use scaled natural stress variables $\hat{\lambda}, \hat{\mu}, \hat{\nu}$ as follows:

$$\lambda = \frac{\hat{\lambda}}{|\mathbf{v}|^2}, \quad \mu = \hat{\mu}, \quad \nu = \hat{\nu} |\mathbf{v}|^2, \quad (2.18)$$

which satisfy the following component equations:

$$\text{Wi} \left[\frac{\partial \hat{\lambda}}{\partial t} + \frac{2\hat{\mu}}{|\mathbf{v}|^2} \left(v \frac{\partial u}{\partial t} - u \frac{\partial v}{\partial t} \right) + |\mathbf{v}|^2 (\mathbf{v} \cdot \nabla) \left(\frac{\hat{\lambda}}{|\mathbf{v}|^2} \right) + 2\hat{\mu} |\mathbf{v}|^2 \nabla \cdot \mathbf{w} \right] \\ + (\hat{\lambda} - 1) + \kappa g_{\hat{\lambda}} = 0, \quad (2.19)$$

$$\text{Wi} \left[\frac{\partial \hat{\mu}}{\partial t} + \left(\frac{\hat{\lambda} - \hat{\nu}}{|\mathbf{v}|^2} \right) \left(u \frac{\partial v}{\partial t} - v \frac{\partial u}{\partial t} \right) + (\mathbf{v} \cdot \nabla) \hat{\mu} + \hat{\nu} |\mathbf{v}|^2 \nabla \cdot \mathbf{w} \right] \\ + \hat{\mu} + \kappa g_{\hat{\mu}} = 0, \quad (2.20)$$

$$\text{Wi} \left[\frac{\partial \hat{\nu}}{\partial t} + \frac{2\hat{\mu}}{|\mathbf{v}|^2} \left(u \frac{\partial v}{\partial t} - v \frac{\partial u}{\partial t} \right) + \frac{1}{|\mathbf{v}|^2} (\mathbf{v} \cdot \nabla) (\hat{\nu} |\mathbf{v}|^2) \right] \\ + (\hat{\nu} - 1) + \kappa g_{\hat{\nu}} = 0, \quad (2.21)$$

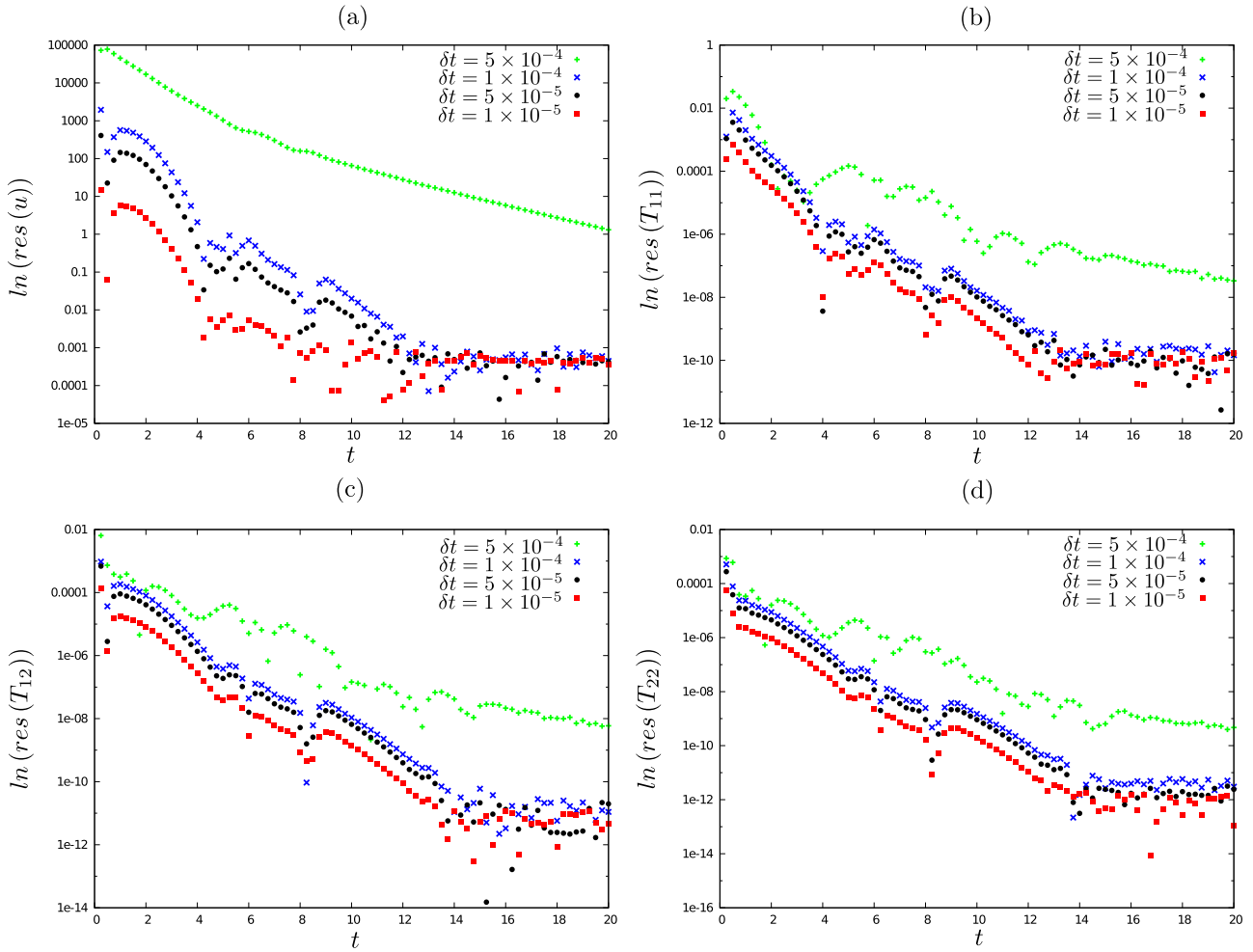


FIG. 4. Time variation of the CSF local residuals of (a) u , (b) T_{11} , (c) T_{12} , and (d) T_{22} near to the singularity for the PTT model using $\beta = 1/2$.

where

$$g_{\hat{\lambda}} = \begin{cases} (\hat{\lambda} + \hat{\nu} - 2)(\hat{\lambda} - 1), & \text{PTT}, \\ [\hat{\lambda}^2 + \hat{\mu}^2], & \text{Giesekus}, \end{cases} \quad (2.22)$$

$$g_{\hat{\mu}} = (\hat{\lambda} + \hat{\nu} - 2)\hat{\mu}, \quad (2.23)$$

$$g_{\hat{\nu}} = \begin{cases} (\hat{\lambda} + \hat{\nu} - 2)(\hat{\nu} - 1), & \text{PTT}, \\ [(\hat{\nu} - 1)^2 + \hat{\mu}^2], & \text{Giesekus}, \end{cases} \quad (2.24)$$

with

$$\begin{aligned} |\mathbf{v}|^2 \nabla \cdot \mathbf{w} &= |\mathbf{v}|^2 \left(\frac{\partial}{\partial x} \left(-\frac{v}{|\mathbf{v}|^2} \right) + \frac{\partial}{\partial y} \left(\frac{u}{|\mathbf{v}|^2} \right) \right) \\ &= \frac{1}{|\mathbf{v}|^2} \left((v^2 - u^2) \left(\frac{\partial v}{\partial x} + \frac{\partial u}{\partial y} \right) + 4uv \frac{\partial u}{\partial x} \right). \end{aligned}$$

The component form of (2.15), adopting Eqs. (2.17) and (2.18), results in the following equations:

$$T_{11} = \frac{(1-\beta)}{Wi} \left(-1 + \frac{1}{|\mathbf{v}|^2} (\hat{\lambda}u^2 - 2\hat{\mu}uv + \hat{\nu}v^2) \right), \quad (2.25)$$

$$T_{12} = \frac{(1-\beta)}{Wi|\mathbf{v}|^2} (\hat{\lambda}uv + \hat{\mu}(u^2 - v^2) - \hat{\nu}uv), \quad (2.26)$$

$$T_{22} = \frac{(1-\beta)}{Wi} \left(-1 + \frac{1}{|\mathbf{v}|^2} (\hat{\lambda}v^2 + 2\hat{\mu}uv + \hat{\nu}u^2) \right), \quad (2.27)$$

with the inverse relationships being

$$\hat{\lambda} - 1 = \frac{Wi}{(1-\beta)|\mathbf{v}|^2} (u^2 T_{11} + 2uv T_{12} + v^2 T_{22}), \quad (2.28)$$

$$\hat{\mu} = \frac{Wi}{(1-\beta)|\mathbf{v}|^2} (-uv T_{11} + (u^2 - v^2) T_{12} + uv T_{22}), \quad (2.29)$$

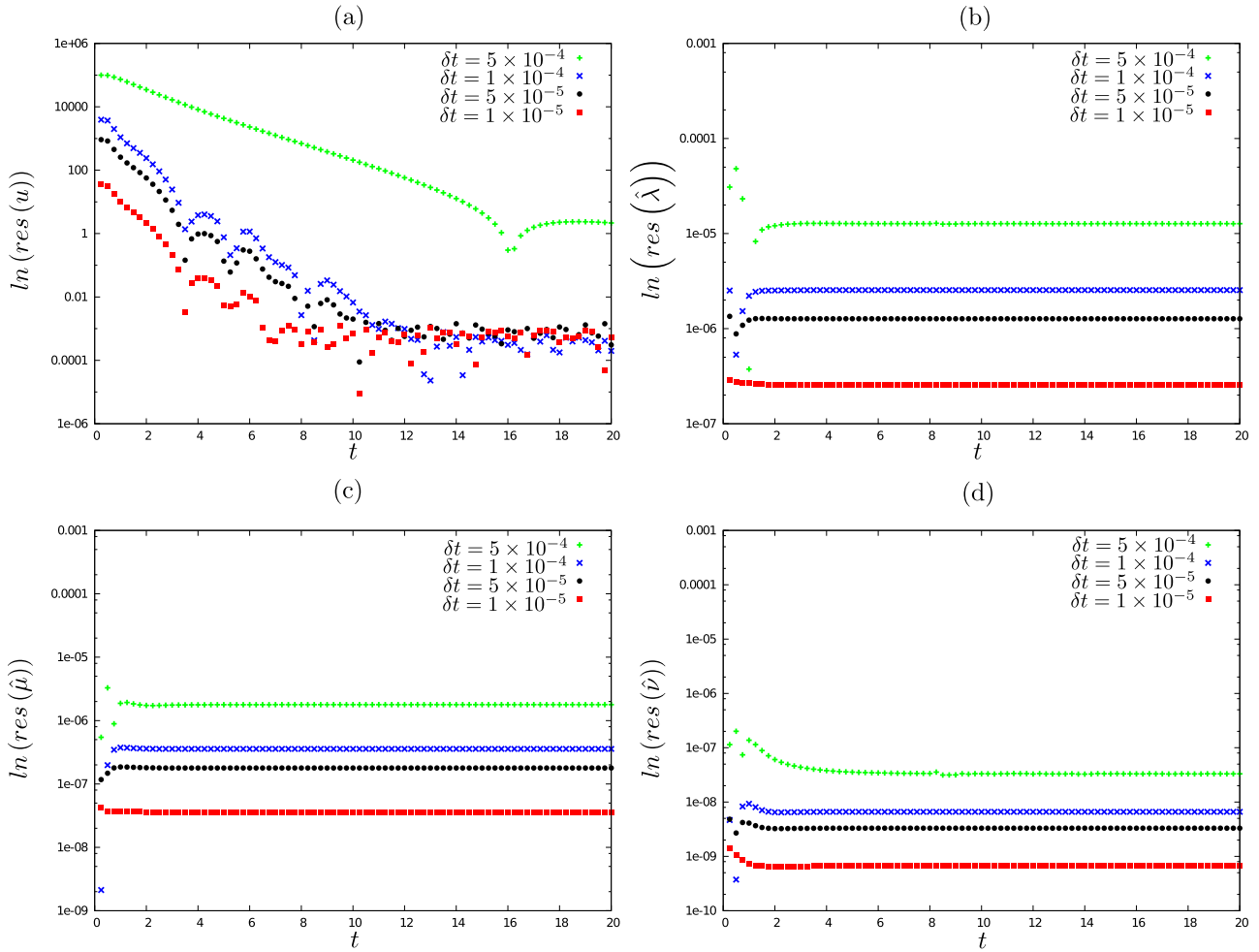


FIG. 5. Time variation of the NSF local residuals of (a) u , (b) $\hat{\lambda}$, (c) $\hat{\mu}$, and (d) $\hat{\nu}$ near to the singularity for the PTT model using $\beta = 1/2$.

$$\hat{v} - 1 = \frac{Wi}{(1-\beta)|\mathbf{v}|^2} (v^2 T_{11} - 2uv T_{12} + u^2 T_{22}). \quad (2.30)$$

We refer to (2.19)–(2.21) as the natural stress formulation (NSF) of the constitutive equations, which may be solved with the momentum equation in the form (2.7) and (2.8) on using (2.25)–(2.27).

A. Flow description

The planar stick-slip geometry is shown schematically in Fig. 1. We have a sudden modification in the boundary condition at the stick-slip transition point where the stress singularity is located. On the solid surface (denoted here as $\partial\Omega_{st}$), we have no-slip boundary condition,

$$\mathbf{v} = \mathbf{0} \quad \text{in} \quad \partial\Omega_{st}, \quad (2.31)$$

while, on the slip surface $\partial\Omega_{sl}$, we have no flow across the surface,

$$v = 0 \quad \text{in} \quad \partial\Omega_{sl} \quad (2.32)$$

and no shear-stress

$$T_{12} + \beta \frac{\partial u}{\partial y} = 0 \quad \text{on} \quad \partial\Omega_{sl}. \quad (2.33)$$

The boundary conditions for the velocity field imposed at the inlet assumes fully developed flow [$u = u(y)$, $v = 0$], while a Neumann homogeneous boundary condition is applied at the outlet. As an initial condition at $t = 0$, the Cartesian extra stress is set as $\mathbf{T} = \mathbf{0}$.

The initial and boundary conditions for the natural stress variables $\hat{\lambda}$, $\hat{\mu}$, and \hat{v} are taken consistent with the Cartesian extra stress variables using (2.28)–(2.30). At the inlet, with $v = 0$ for fully developed flow, we have

$$\begin{aligned} \hat{\lambda} &= \left[\frac{Wi}{(1-\beta)} T_{11} + 1 \right] / u^2, & \hat{\mu} &= \frac{Wi}{(1-\beta)} T_{12}, \\ \hat{v} &= u^2 \left[\frac{Wi}{(1-\beta)} T_{22} + 1 \right], \end{aligned} \quad (2.34)$$

while at the outlet, a homogeneous Neumann condition is employed. For the stick and slip regions, the conditions (2.31) and (2.32) are adopted together with the equivalent of (2.33) being

$$\frac{(1-\beta)}{Wi} \hat{\mu} + \beta \frac{\partial u}{\partial y} = 0 \quad \text{on} \quad \partial\Omega_{sl}. \quad (2.35)$$

The initialization $\hat{\lambda} = \hat{v} = 1$ and $\hat{\mu} = 0$ at $t = 0$ completes the specification of the NS variables.

We remark that at the inlet (and also initially at $t = 0$), specifying the three Cartesian extra-stresses or the three natural stress variables is sufficient to determine the two characteristic quantities required for well-posedness of the Partial Differential Equations (PDE) system (2.1)–(2.3).^{41,42} The two characteristic quantities here are

$$\det \left(\mathbf{T} + \frac{(1-\beta)}{Wi} \mathbf{I} \right) = \frac{(1-\beta)^2}{Wi^2} (\hat{\lambda} \hat{v} - \hat{\mu}^2)$$

and

$$(\mathbf{v}^\perp)^T \left(\mathbf{T} + \frac{(1-\beta)}{Wi} \mathbf{I} \right) \mathbf{v}^\perp = \frac{(1-\beta)}{Wi} |\mathbf{v}|^2 \hat{v},$$

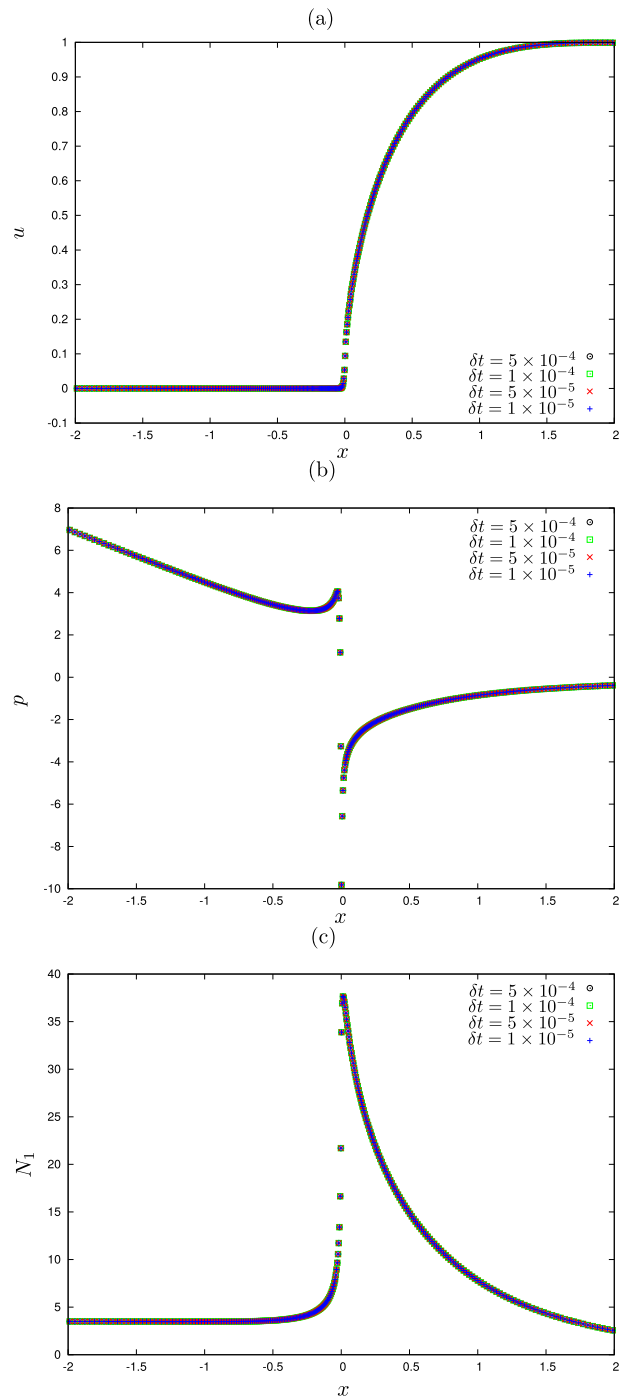


FIG. 6. Profiles of (a) u , (b) p , and (c) N_1 along the horizontal line $y = 1$ for the PTT model using different time steps.

where $\mathbf{v}^\perp = |\mathbf{v}|^2 \mathbf{w}$, which are transported along the characteristics associated with the constitutive equation (2.3). In the steady case, the characteristics are streamlines, while they are particle paths in the unsteady case. The classification analysis of

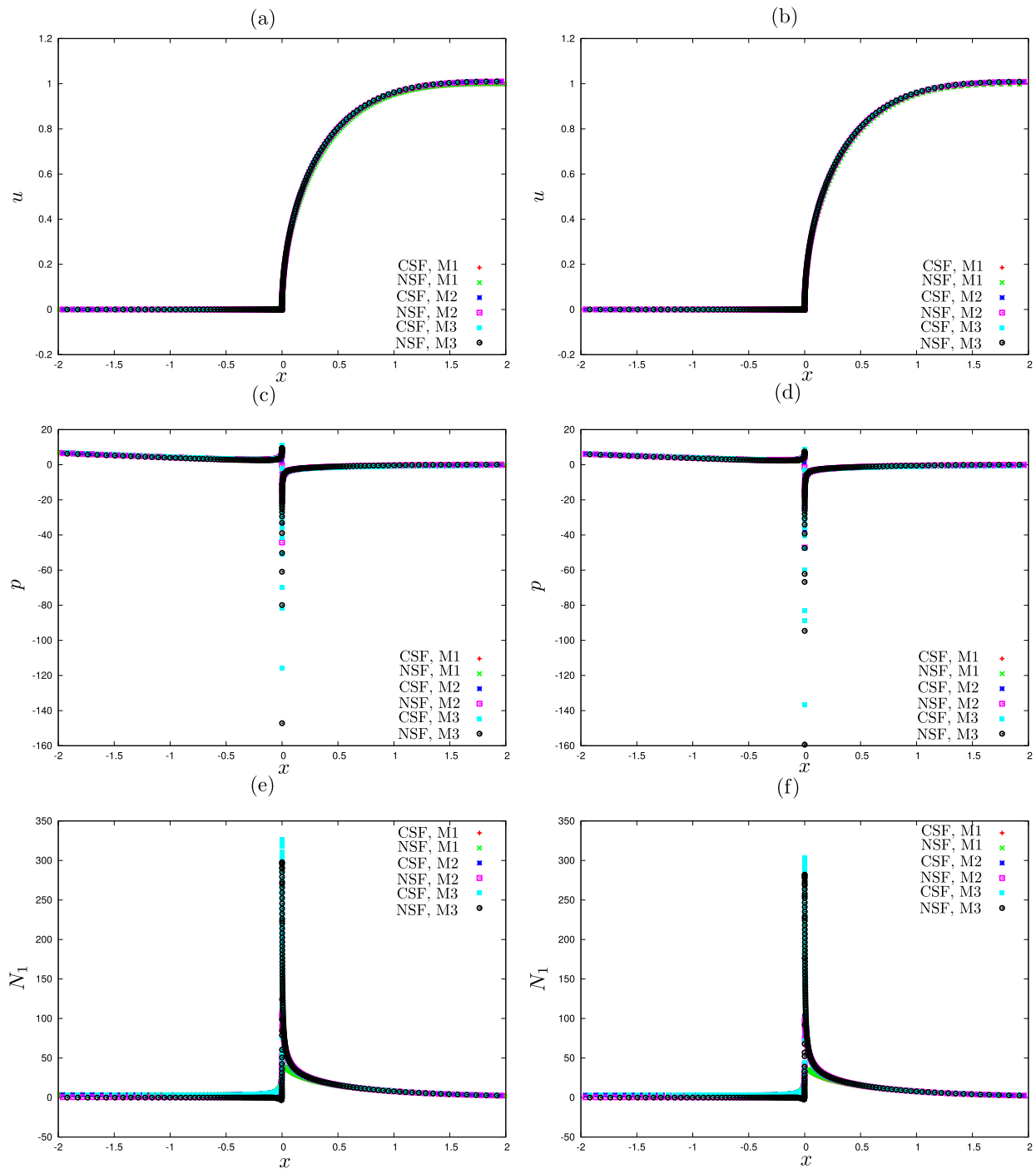


FIG. 7. Profiles of (a) u (PTT), (b) u (Giesekus), (c) p (PTT), (d) p (Giesekus), (e) N_1 (PTT), and (f) N_1 (Giesekus) along the horizontal line $y = 1$.

Refs. 41 and 42 for the UCM model still pertains for the PTT and Giesekus models in the forms presented here, although the transport equations for the characteristic quantities necessarily change.

B. Overview of the numerical method

We implement the numerical scheme in a finite-difference framework. The algorithm has two main steps:

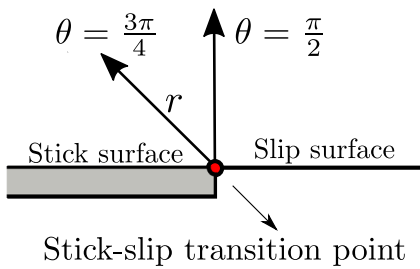


FIG. 8. Illustration of the selected angles for studying the asymptotic behavior near the stick-slip transition point.

1. Computation of velocity and pressure fields: Based on a semi-implicit scheme, Eqs. (2.1) and (2.2) are uncoupled via an incremental projection method.⁴³ In this strategy, the momentum equation (2.2) is solved for a tentative velocity field $\tilde{\mathbf{v}}^{(n+1)}$

considering an implicit discretization for the viscous term, while the convective terms, pressure gradient and divergence of the stress tensor, are treated in an explicit manner, e.g.,

$$\frac{\tilde{\mathbf{v}}^{(n+1)}}{\delta t} - \frac{\beta}{Re} \nabla^2 \tilde{\mathbf{v}}^{(n+1)} = \frac{\mathbf{v}^{(n)}}{\delta t} - ((\mathbf{v} \cdot \nabla) \mathbf{v})^{(n)} - \frac{1}{Re} \nabla p^{(n)} + \frac{1}{Re} \nabla \cdot (\mathbf{T})^{(n)}, \quad (2.36)$$

where δt is the time step. Once the intermediate velocity field is obtained, the final velocity field is updated based on the Helmholtz-Hodge decomposition⁴⁴

$$\mathbf{v}^{(n+1)} = \tilde{\mathbf{v}}^{(n+1)} - \nabla \phi^{(n+1)}, \quad (2.37)$$

where the final pressure field is incremented by an iterative process^{45,46}

$$p^{(n+1)} = p^{(n)} + \frac{Re}{\delta t} \phi^{(n+1)}, \quad (2.38)$$

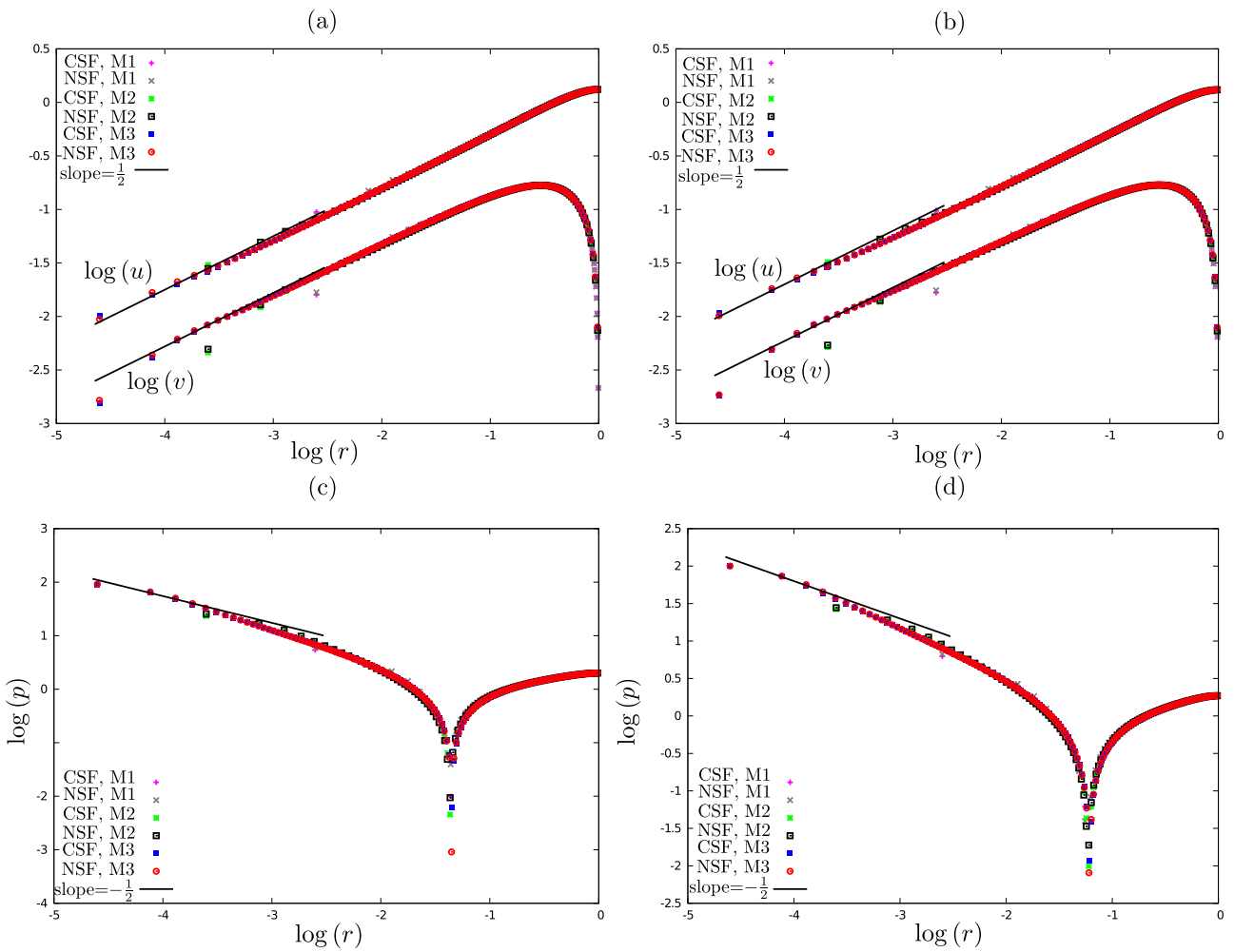


FIG. 9. Asymptotic variation near the stick-slip transition point of (a) u , v (PTT), (b) u , v (Giesekus), (c) p (PTT), and (d) p (Giesekus) along the line $\theta = \pi/2$ with $\beta = 1/2$ and $Wi = 1$.

with ϕ being an intermediate pressure which needs to be previously computed. This computation is done by solving the Poisson-like equation,

$$\nabla^2 \phi^{(n+1)} = \nabla \cdot \tilde{\mathbf{v}}^{(n+1)}. \quad (2.39)$$

To solve the stick-slip problem by the incremental projection method, it is necessary to construct correct boundary conditions for ϕ , respecting the boundary conditions imposed for the velocity field \mathbf{v} in the two regions of the domain:

- Boundary conditions for the Poisson equation in the stick region: As the no-slip boundary condition applies for the velocity field, we have imposed the classical homogeneous Neumann boundary condition for the intermediate pressure, i.e.,

$$\frac{\partial \phi}{\partial y} = 0 \quad \text{in } \partial\Omega_{st}. \quad (2.40)$$

- Boundary conditions for the Poisson equation in the slip region: We propose a specific boundary condition for the intermediate pressure when the projection method is applied under slip conditions. The normal stress condition is

$$\mathbf{n} \cdot [-p\mathbf{I} + 2\beta\mathbf{D} + \mathbf{T}] \cdot \mathbf{n}^T = 0, \quad (2.41)$$

where \mathbf{n} denotes the outward unit normal vector to the boundary $\partial\Omega_{sl}$. Equation (2.41) is commonly used as a free surface boundary condition for solving interface problems (see in Ref. 47). Imposing Eq. (2.41) on the free slip surface and considering the fixed normal vector $\mathbf{n} = [0, 1]$, we obtain

$$-p + 2\beta \frac{\partial v}{\partial y} + T_{22} = 0. \quad (2.42)$$

Using the continuity equation (2.6), (2.42) may be rewritten as

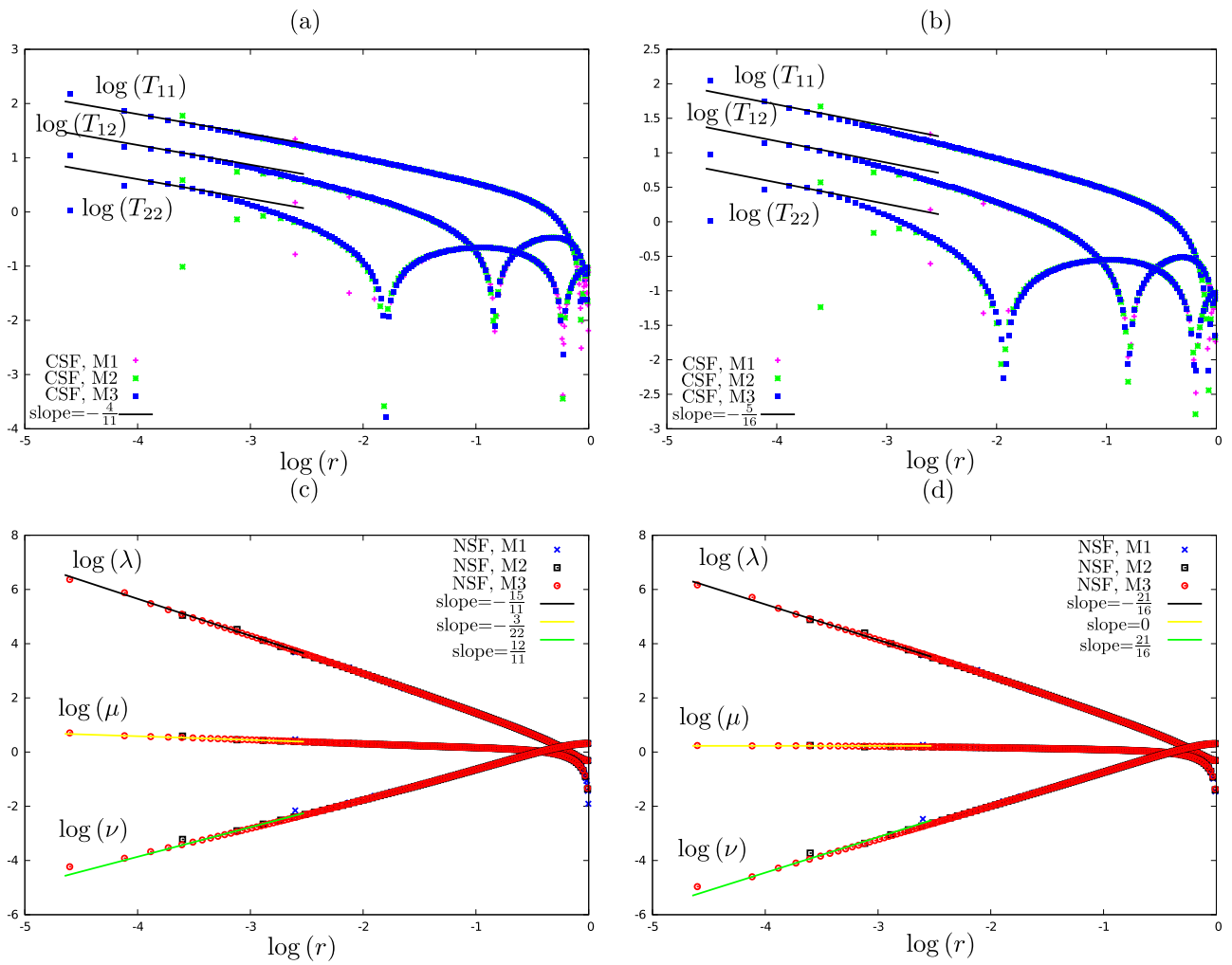


FIG. 10. Asymptotic variation near the stick-slip transition point of (a) T_{11} , T_{12} , T_{22} (PTT), (b) T_{11} , T_{12} , T_{22} (Giesekus), (c) λ , μ , ν (PTT), and (d) λ , μ , ν (Giesekus) along the line $\theta = \pi/2$ with $\beta = 1/2$ and $Wi = 1$.

$$-p - 2\beta \frac{\partial u}{\partial x} + T_{22} = 0. \quad (2.43)$$

According to the ideas of the semi-implicit version of the marker-and-cell algorithm,⁴³ Eq. (2.43) can be used to compute the pressure field at the free surface by an iterative process imposing the following time discretization:

$$-p^{(n+1)} = 2\beta \frac{\partial u^{(n+1)}}{\partial x} - T_{22}^{(n)}. \quad (2.44)$$

In the present work, Eq. (2.44) is combined with the update velocity (2.37) and pressure (2.38), resulting in a specific boundary condition for ϕ on the free slip surface,

$$\frac{Re}{\delta t} \phi^{(n+1)} - 2\beta \frac{\partial^2 \phi^{(n+1)}}{\partial x^2} = -2\beta \frac{\partial \bar{u}^{(n+1)}}{\partial x} + T_{22}^{(n)} - p^{(n)} \text{ in } \partial\Omega_{sl}. \quad (2.45)$$

- Computation of the non-Newtonian tensor: After obtaining the final velocity and pressure fields, the final value for the extra stress tensor $\mathbf{T}^{(n+1)}$ is computed according to the two stress formulation:

- Cartesian stress formulation: Equation (2.3) is discretized in the following explicit manner:

$$\begin{aligned} \frac{\mathbf{T}^{(n+1)} - \mathbf{T}^{(n)}}{\delta t} &= \frac{1}{Wi} \left(-\mathbf{T}^{(n)} - (\mathbf{v}^{(n+1)} \cdot \nabla) \mathbf{T}^{(n)} \right. \\ &\quad \left. + (\nabla \mathbf{v}^{(n+1)}) \mathbf{T}^{(n)} + \mathbf{T}^{(n)} (\nabla \mathbf{v}^{(n+1)})^T \right) \\ &\quad - \frac{\kappa}{1-\beta} \mathbf{g}(\mathbf{T}^{(n)}) + 2 \frac{1-\beta}{Wi} \mathbf{D}^{(n)}, \end{aligned} \quad (2.46)$$

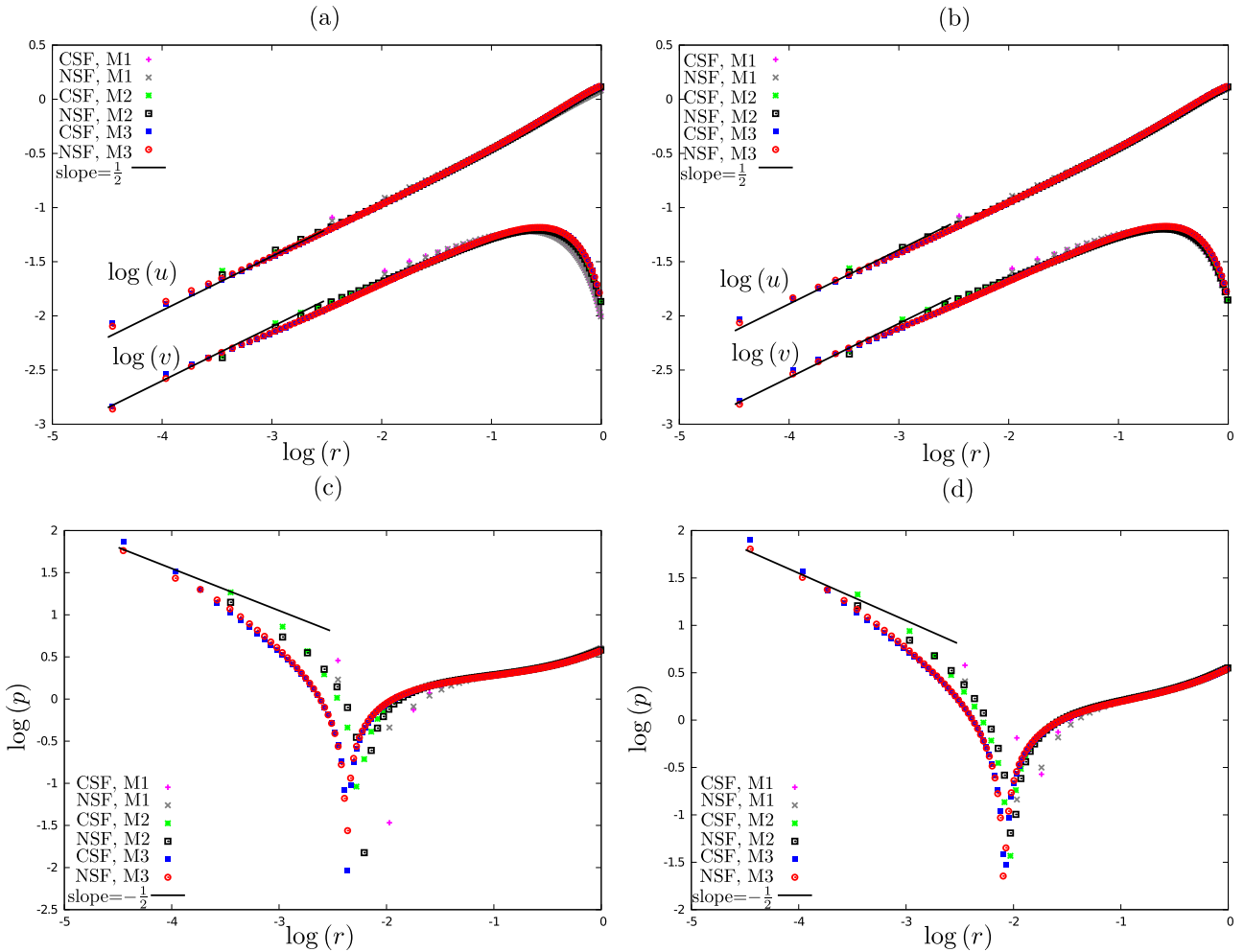


FIG. 11. Asymptotic variation near the stick-slip transition point of (a) u , v (PTT), (b) u , v (Giesekus), (c) p (PTT), and (d) p (Giesekus) along the line $\theta = 3\pi/4$ with $\beta = 1/2$ and $Wi = 1$.

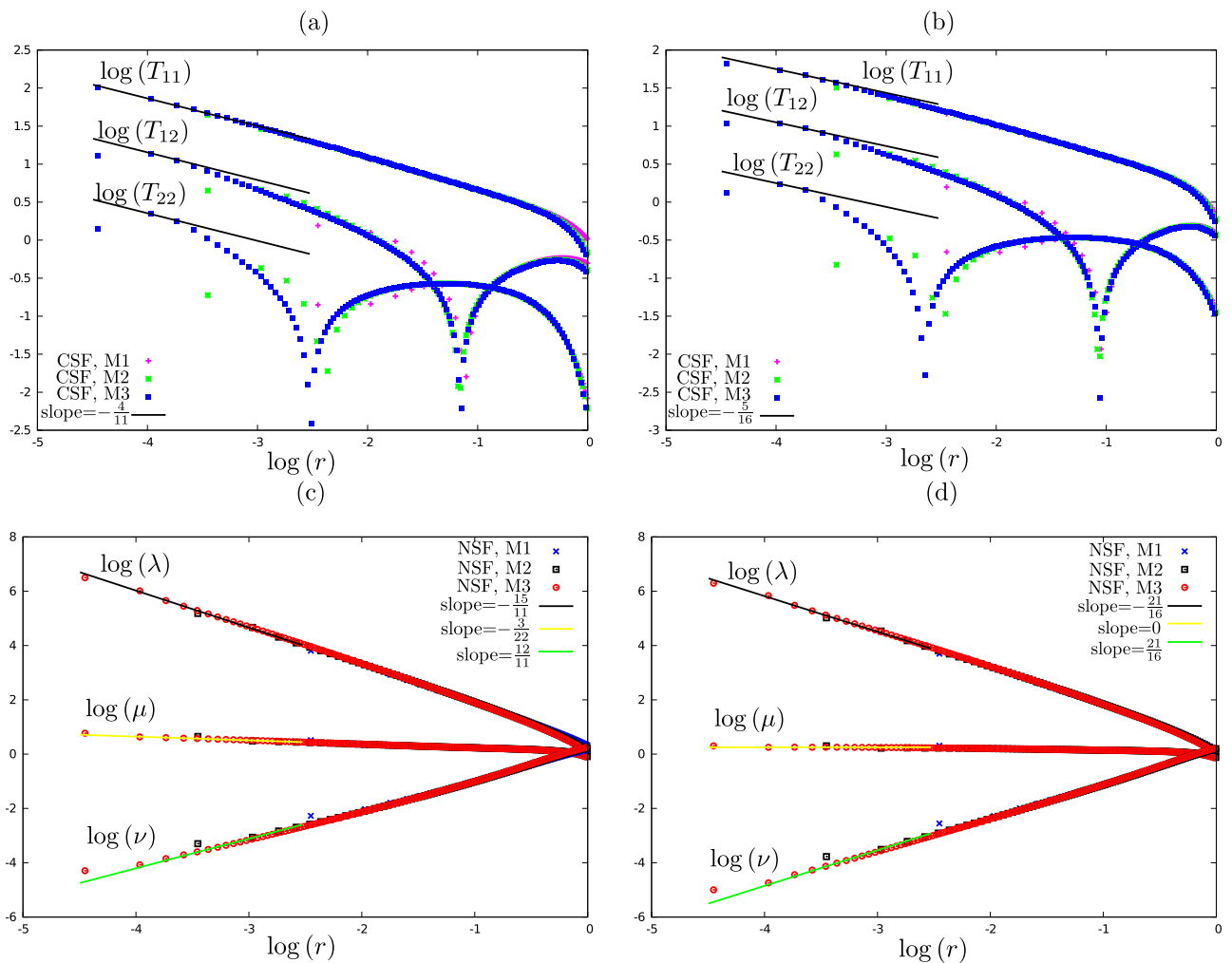


FIG. 12. Asymptotic variation near the stick-slip transition point of (a) T_{11} , T_{12} , T_{22} (PTT), (b) T_{11} , T_{12} , T_{22} (Giesekus), (c) λ , μ , ν (PTT), and (d) λ , μ , ν (Giesekus) along the line $\theta = 3\pi/4$ with $\beta = 1/2$ and $Wi = 1$.

TABLE II. Estimate values of C_0 , C_1 , C_2 , and C_3 as well as radial distances (4.10) for PTT and Giesekus models with $Wi = 1$, $\kappa = 0.1$ and fractional viscosity cases $\beta = 1/2$ and $\beta = 1/9$.

Model	C_0	C_1	C_2	C_3	r_{11}	r_{12}	r_{22}
Newtonian	0.692
$\beta = 1/2$							
PTT	0.745	1.18	1.17	3.86	9×10^{-7}	3×10^{-3}	4.8
Giesekus	0.780	1.30	1.53	5.45	4×10^{-5}	1×10^{-2}	2.8
$\beta = 1/9$							
PTT	0.712	1.13	1.26	4.35	9×10^{-16}	3×10^{-12}	5×10^{-9}
Giesekus	0.817	1.30	1.62	5.83	7×10^{-13}	3×10^{-10}	6×10^{-8}

where $\mathbf{g}(\mathbf{T}^{(n)})$ is constructed selecting the fluid model as was described in Eq. (2.4). Therefore, the components $(T_{11}^{n+1}, T_{12}^{n+1}, T_{22}^{n+1})$ are then computed directly from Eq. (2.46).

- Natural stress formulation: The first stage for this formulation is the solution of Eqs. (2.19)–(2.21) using an explicit time discretization. For example, Eq. (2.19) can be written as

$$\begin{aligned} \frac{\hat{\lambda}^{(n+1)} - \hat{\lambda}^{(n)}}{\delta t} &= -\frac{1}{Wi} (\hat{\lambda}^{(n)} - 1) - \frac{1}{Wi} \kappa g_{\hat{\lambda}^{(n)}} - 2\hat{\mu}^{(n)} |\mathbf{v}^{(n+1)}|^2 \\ &\times \nabla \cdot \mathbf{w}^{(n+1)} - \frac{2\hat{\mu}^{(n)}}{(|\mathbf{v}^{(n+1)}|^2 + tol)} \\ &\times \left(v^{(n+1)} \frac{u^{(n+1)} - u^{(n)}}{\delta t} - u^{(n+1)} \frac{v^{(n+1)} - v^{(n)}}{\delta t} \right) \\ &- |\mathbf{v}^{(n+1)}|^2 (\mathbf{v}^{(n+1)} \cdot \nabla) \left(\frac{\hat{\lambda}^{(n)}}{(|\mathbf{v}^{(n+1)}|^2 + tol)} \right), \end{aligned} \quad (2.47)$$

where

$$\begin{aligned} |\mathbf{v}^{(n+1)}|^2 \nabla \cdot \mathbf{w}^{(n+1)} &= \frac{1}{|\mathbf{v}^{(n+1)}|^2 + tol} \left(((v^{(n+1)})^2 - (u^{(n+1)})^2) \right. \\ &\times \left(\frac{\partial v^{(n+1)}}{\partial x} + \frac{\partial u^{(n+1)}}{\partial y} \right) \\ &+ 4u^{(n+1)}v^{(n+1)} \frac{\partial u^{(n+1)}}{\partial x} \Big). \end{aligned} \quad (2.48)$$

The tolerance $tol = 10^{-6}$ is imposed for regularization in order to avoid numerical division by zero in domain regions where the velocity field vanishes.³³ Equations (2.20) and (2.21) are discretized in a similar manner, resulting in the values for $\hat{\mu}^{(n+1)}$ and $\hat{\nu}^{(n+1)}$. Obtained the NS variables in level time $(n+1)$, we can use the relationships Eqs. (2.25)–(2.27) to compute the final components $(T_{11}^{n+1}, T_{12}^{n+1}, T_{22}^{n+1})$ of the extra-stress tensor.

The algorithms of the numerical schemes for CSF and NSF are summarized in the flowchart in Fig. 2.

C. Nonuniform mesh discretization

To capture the effect of the singularity, we have applied a stretching strategy for refining the mesh elements around the stick-slip transition point, as illustrated in Fig. 3. In particular, we use three nonuniform meshes, M1, M2, and M3. Details for the minimum value for the space steps Δx_{min} and Δy_{min} being given in Table I.

III. CONVERGENCE RESULTS

We demonstrate the capability of the numerical scheme for solving the stick-slip problem by considering the complete system of governing equations for the PTT and Giesekus models using both the Cartesian and natural stress formulations. We first validate the

scheme through a mesh refinement study by considering profiles of the pressure, first normal stress difference, and velocity in two cross sections of the domain. After this, we compare numerical results for the polymer stress near to the singularity with the predicted

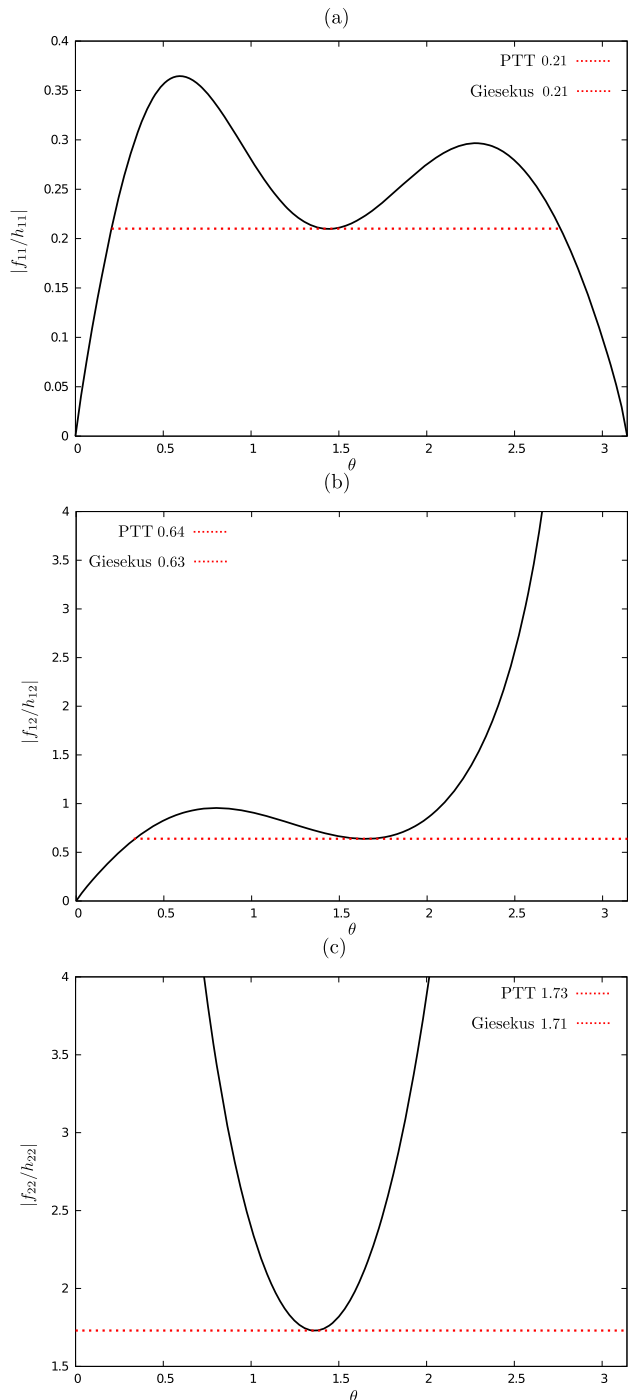


FIG. 13. Variation of (a) $|f_{11}/h_{11}|$, (b) $|f_{12}/h_{12}|$, and (c) $|f_{22}/h_{22}|$ with θ for PTT $n_1 = -10/11$. The curves for Giesekus $n_1 = -7/8$ are almost identical.

theoretical asymptotic behaviors. In all simulations in this section, we use parameter values of $Re = 0.01$, $Wi = 1$, $\kappa = 0.1$, and $\beta = 1/2$. The verification of the numerical schemes for Newtonian flow can be found in Appendix A.

A. Numerical study of temporal convergence

Here, we confirm temporal convergence of the schemes as the time step reduces. Since the main purpose of the current work is

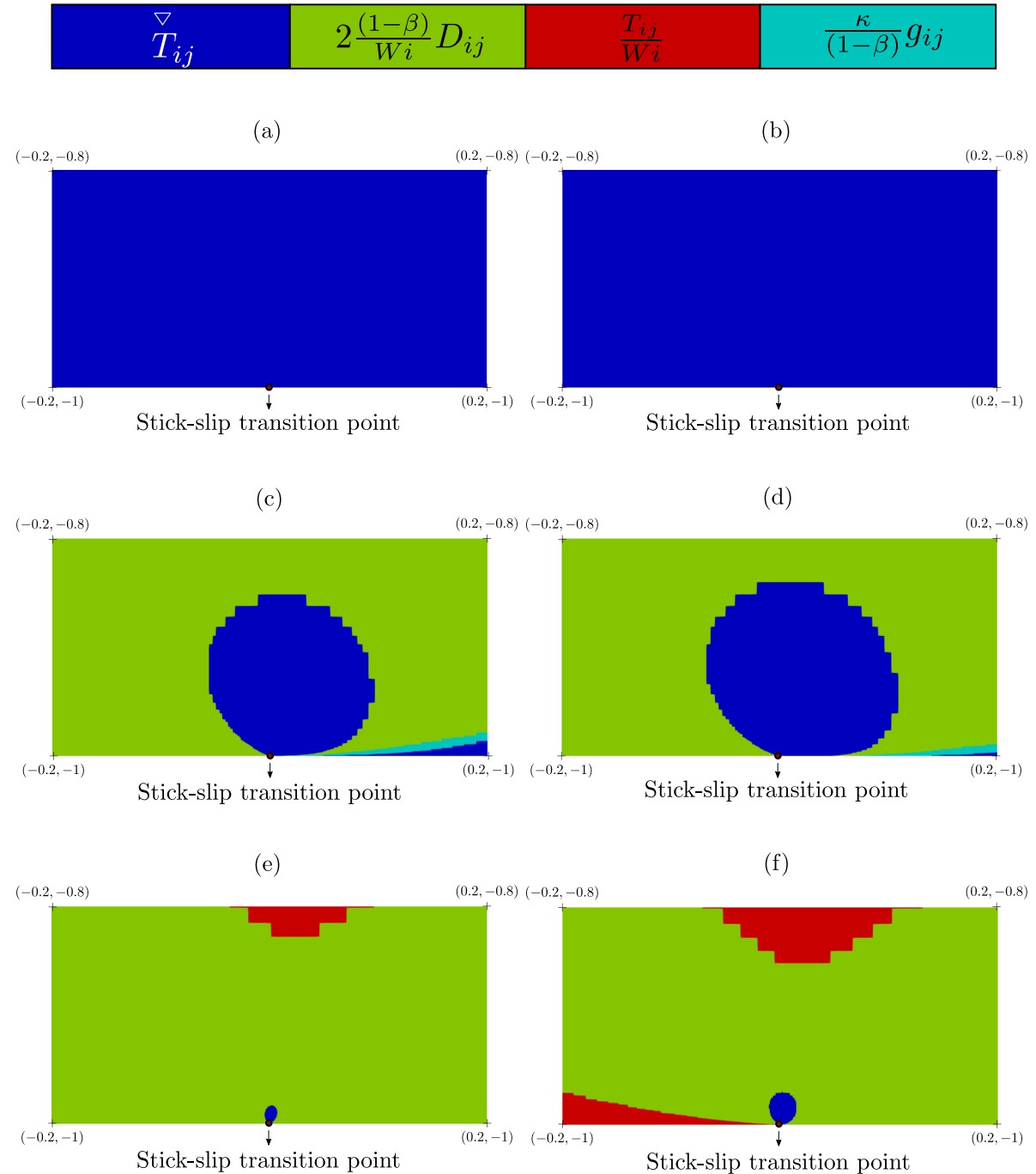


FIG. 14. Dominance of the groups of terms (4.12) for components (a) $ij = 11$ (PTT), (b) $ij = 11$ (Giesekus), (c) $ij = 12$ (PTT), (d) $ij = 12$ (Giesekus), (e) $ij = 22$ (PTT), and (f) $ij = 22$ (Giesekus) within the Cartesian constitutive equation using $\beta = 1/2$ and $Wi = 1$.

related to the numerical behavior of variables around the singularity, temporal convergence is studied through the local residual as a time function at a control point located in the closest cell to the singularity.

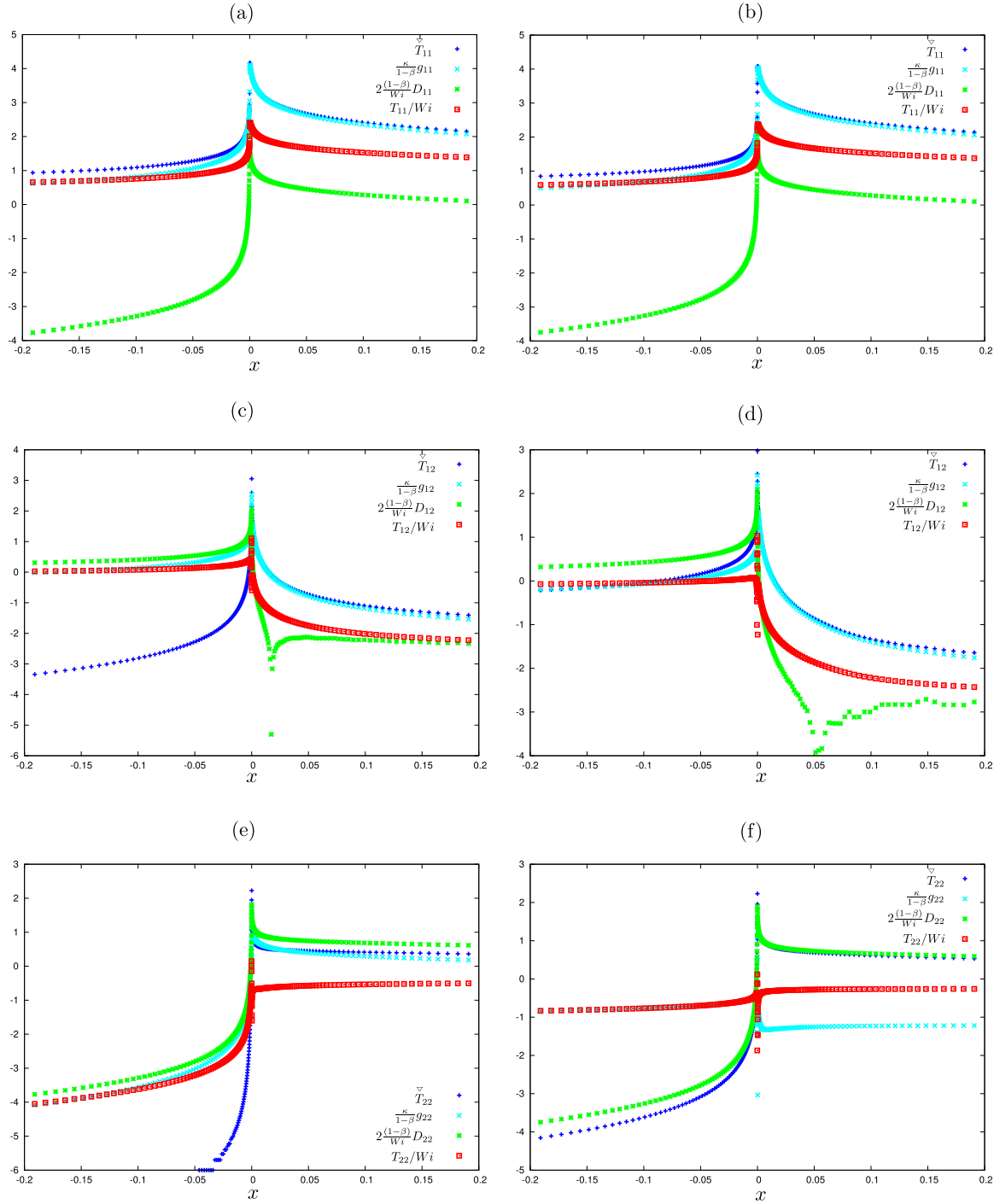


FIG. 15. Dominance of the groups of terms (4.12) for components (a) $j = 11$ (PTT), (b) $j = 11$ (Giesekus), (c) $j = 12$ (PTT), (d) $j = 12$ (Giesekus), (e) $j = 22$ (PTT), and (f) $j = 22$ (Giesekus) within the Cartesian constitutive equation using $\beta = 1/2$ and $Wi = 1$.

The local residuals for the velocity in the x direction, the component 11 of the extra stress tensor and the $\hat{\lambda}$ NS variable are, respectively, evaluated as

$$\begin{aligned} \text{res}(u)|_P &= \frac{u^{(n+1)} - u^{(n)}}{\delta t} \Big|_P + \left(u \frac{\partial u}{\partial x} + v \frac{\partial u}{\partial y} \right) \Big|_P^{(n+1)} + \frac{1}{\text{Re}} \frac{\partial p}{\partial x} \Big|_P^{(n+1)} \\ &\quad - \frac{\beta}{\text{Re}} \left(\frac{\partial^2 u}{\partial x^2} + \frac{\partial^2 u}{\partial y^2} \right) \Big|_P^{(n+1)} - \frac{1}{\text{Re}} \left(\frac{\partial T_{11}}{\partial x} - \frac{\partial T_{12}}{\partial y} \right) \Big|_P^{(n+1)}, \end{aligned} \quad (3.1)$$

$$\begin{aligned} \text{res}(T_{11})|_P &= \frac{T_{11}^{(n+1)} - T_{11}^{(n)}}{\delta t} \Big|_P + \left(u \frac{\partial T_{11}}{\partial x} + v \frac{\partial T_{11}}{\partial y} \right) \Big|_P^{(n+1)} \\ &\quad - \left(2 \frac{\partial u}{\partial x} T_{11} + 2 \frac{\partial u}{\partial y} T_{12} \right) \Big|_P^{(n+1)} + \frac{\kappa}{(1-\beta)} g_{11} \Big|_P^{(n+1)} \\ &\quad - \frac{2}{\text{Wi}} (1-\beta) \frac{\partial u}{\partial x} \Big|_P^{(n+1)}, \end{aligned} \quad (3.2)$$

and

$$\begin{aligned} \text{res}(\hat{\lambda})|_P &= \frac{\hat{\lambda}^{(n+1)} - \hat{\lambda}^{(n)}}{\delta t} \Big|_P + \left(\frac{2\hat{\mu}}{|\mathbf{v}|^2} \left(v \frac{\partial u}{\partial t} - u \frac{\partial v}{\partial t} \right) \right) \Big|_P^{(n+1)} \\ &\quad + \left(|\mathbf{v}|^2 (\mathbf{v} \cdot \nabla) \left(\frac{\hat{\lambda}}{|\mathbf{v}|^2} \right) \right) \Big|_P^{(n+1)} + \left(2\hat{\mu} |\mathbf{v}|^2 \nabla \cdot \mathbf{w} \right) \Big|_P^{(n+1)} \\ &\quad + \left(\frac{1}{\text{Wi}} (\hat{\lambda} - 1) + \frac{\kappa}{\text{Wi}} g_{\hat{\lambda}} \right) \Big|_P^{(n+1)}, \end{aligned} \quad (3.3)$$

where g_{11} is computed from Eq. (2.12) while $g_{\hat{\lambda}}$ is obtained from Eq. (2.22). The local residuals for the other components of the extra stress tensor and for the remaining NS variables can be constructed in a similar manner. In particular, the investigation will be done for the PTT model (results for Giesekus being similar) on the coarse mesh M1 and varying the time step as $\delta t = 5 \times 10^{-4}, 1 \times 10^{-4}, 5 \times 10^{-5}, 1 \times 10^{-5}$.

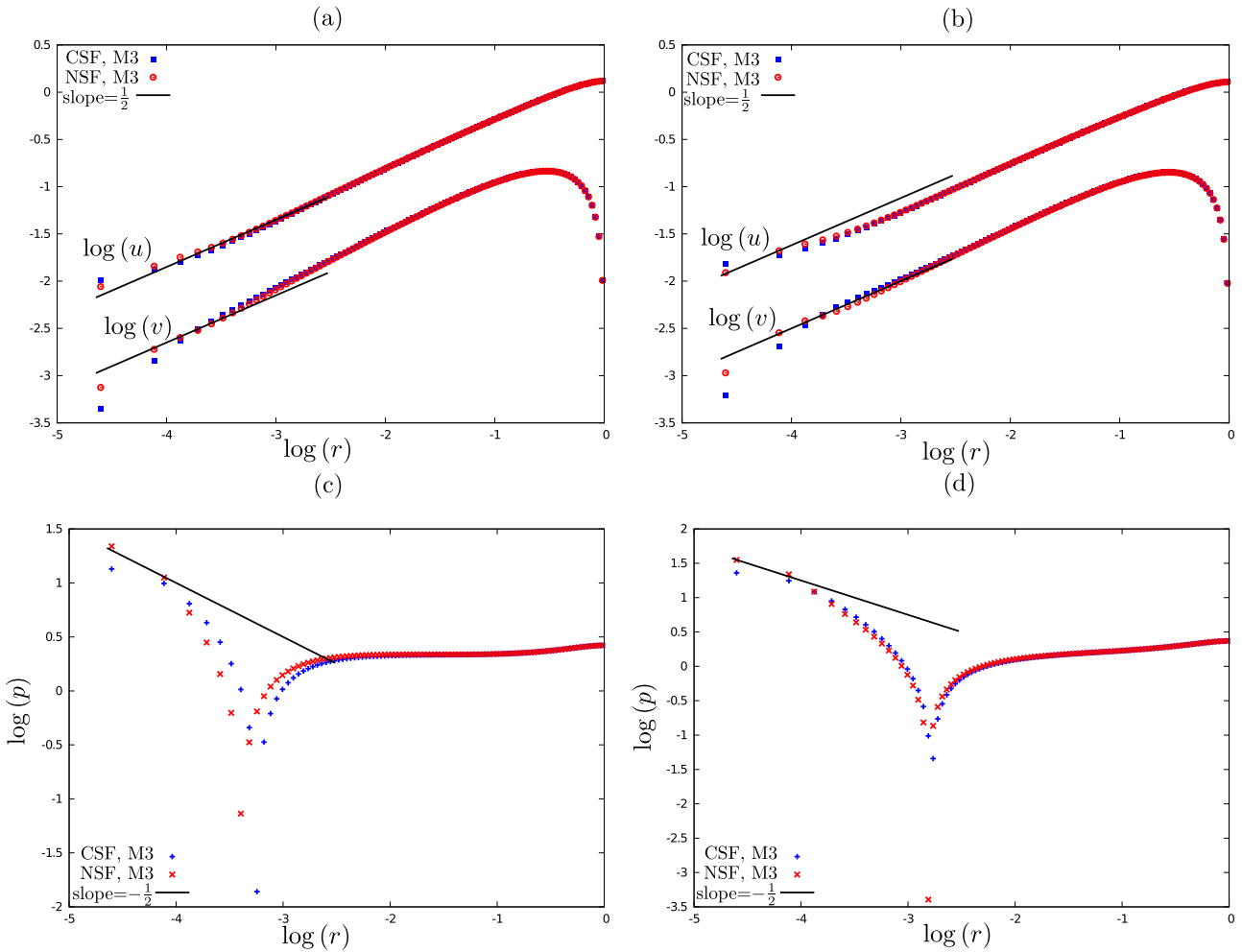


FIG. 16. Asymptotic variation near the stick-slip transition point of (a) u, v (PTT), (b) u, v (Giesekus), (c) p (PTT), and (d) p (Giesekus) along the line $\theta = \pi/2$ considering the half-length $L = 4$ with $\beta = 1/9$.

Figures 4 and 5 present the time variation of local residuals on a logarithm scale for CSF and NSF, respectively. They confirm temporal convergence for both formulations, provided a sufficiently small time step of $\delta t = 1 \times 10^{-4}$ or smaller is used. However, for the largest time step shown, $\delta t = 5 \times 10^{-4}$, the local residual for Eq. (3.1) is still large compared to those of the smaller time steps and in fact, the use of a time step greater than $\delta t = 5 \times 10^{-4}$ leads to a complete breakdown of the code for both formulations. Therefore, in order to capture the expected behavior of the stress singularities, in this work, we have adopted small time step values for all meshes, for instance, $\delta t = 1 \times 10^{-5}$ for M2 and $\delta t = 5 \times 10^{-6}$ for M3. As a consequence of this Courant-Friedrichs-Lowy (CFL) limitation, the central processing unit (CPU) time can considerably increase in the application of very refined meshes, such as those used in Ref. 38 in the steady case. Interestingly, these residual plots also illustrate the significant rate of convergence improvement for the NS variables

over the CS variables, emphasizing that the two formulations behave in fundamentally different ways.

B. Numerical investigation of the profiles

Initially, we confirm temporal convergence for the velocity component u , the pressure field p , and the first normal stress difference $N_1 = T_{11} - T_{22}$ along the line $y = 1$. **Figure 6** presents results for PTT using CSF on the coarse mesh M1 for the same time steps adopted in Sec. III A. The temporal convergence behavior for Giesekus is similar.

A mesh refinement study is now employed along the line $y = 1$ that contains the stick-slip transition point. Numerical convergence results for the velocity component u are presented in Figs. 7(a) and 7(b) for PTT and Giesekus, respectively, and show no significant difference between the formulations. However, such a

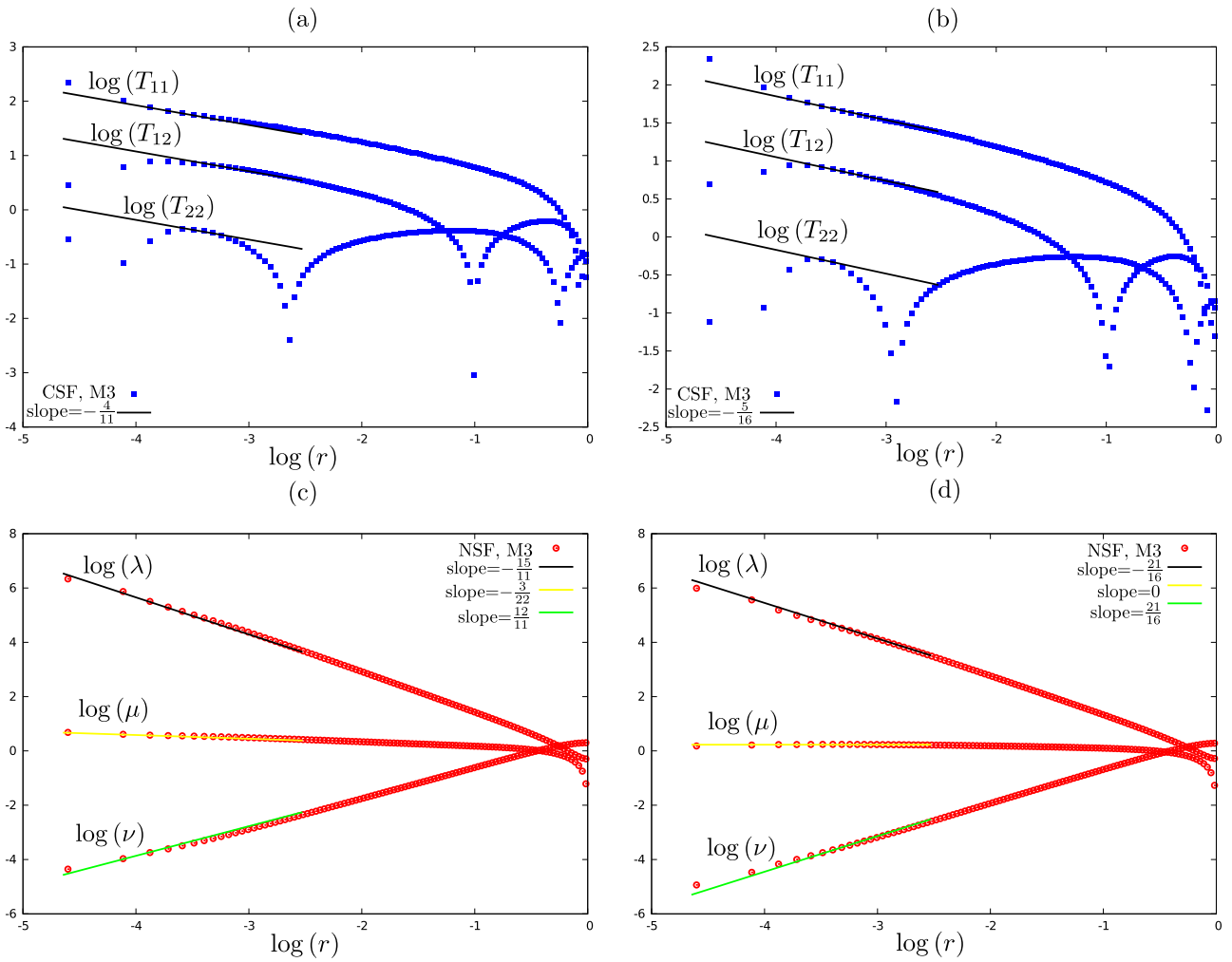


FIG. 17. Asymptotic variation near the stick-slip transition point of (a) T_{11} , T_{12} , T_{22} (PTT), (b) T_{11} , T_{12} , T_{22} (Giesekus), (c) λ , μ , ν (PTT), and (d) λ , μ , ν (Giesekus) along the line $\theta = \pi/2$ considering the half-length $L = 4$ with $\beta = 1/9$.

difference is apparent for p and N_1 , as shown in Figs. 7(c) and 7(d) and Figs. 7(e) and 7(f), respectively. Noticeable is that the minimum pressure is significantly lower for NSF on M3 than for CSF. Figures 7(e) and 7(f) give the distribution of N_1 along the line $y = 1$. Faraway of the stick-slip transition point, mesh refinement confirms numerical convergence of the results in all cases. However, around the singularity, the peak values of the first normal stress difference increase significantly as the mesh is refined. These behaviors are similar to those observed in Refs. 36 and 38 for the PTT model with $\beta = 0$.

IV. STRESS SINGULARITY RESULTS

We now compare numerical results with the theoretical asymptotic results, including a numerical investigation of the boundary layers. We explore the results for a range of solvent viscosities and Weissenberg numbers.

A. Numerical comparison with the asymptotic results

The asymptotic results in Evans *et al.*,²⁹ predict that the solvent stress, velocity, and pressure fields behave, respectively, as

$$\mathbf{T}^s \sim r^{-\frac{1}{2}}, \quad \mathbf{v} \sim r^{\frac{1}{2}}, \quad \text{and} \quad p \sim r^{-\frac{1}{2}}, \quad (4.1)$$

while for the polymer stress, it is expected that

$$\mathbf{T} \sim \begin{cases} r^{-\frac{4}{11}}, & \text{PTT}, \\ r^{-\frac{5}{16}}, & \text{Giesekus}, \end{cases} \quad (4.2)$$

where r is the radial distance from the singularity and multiplicative constants have been omitted. In particular, for the NS variables, the

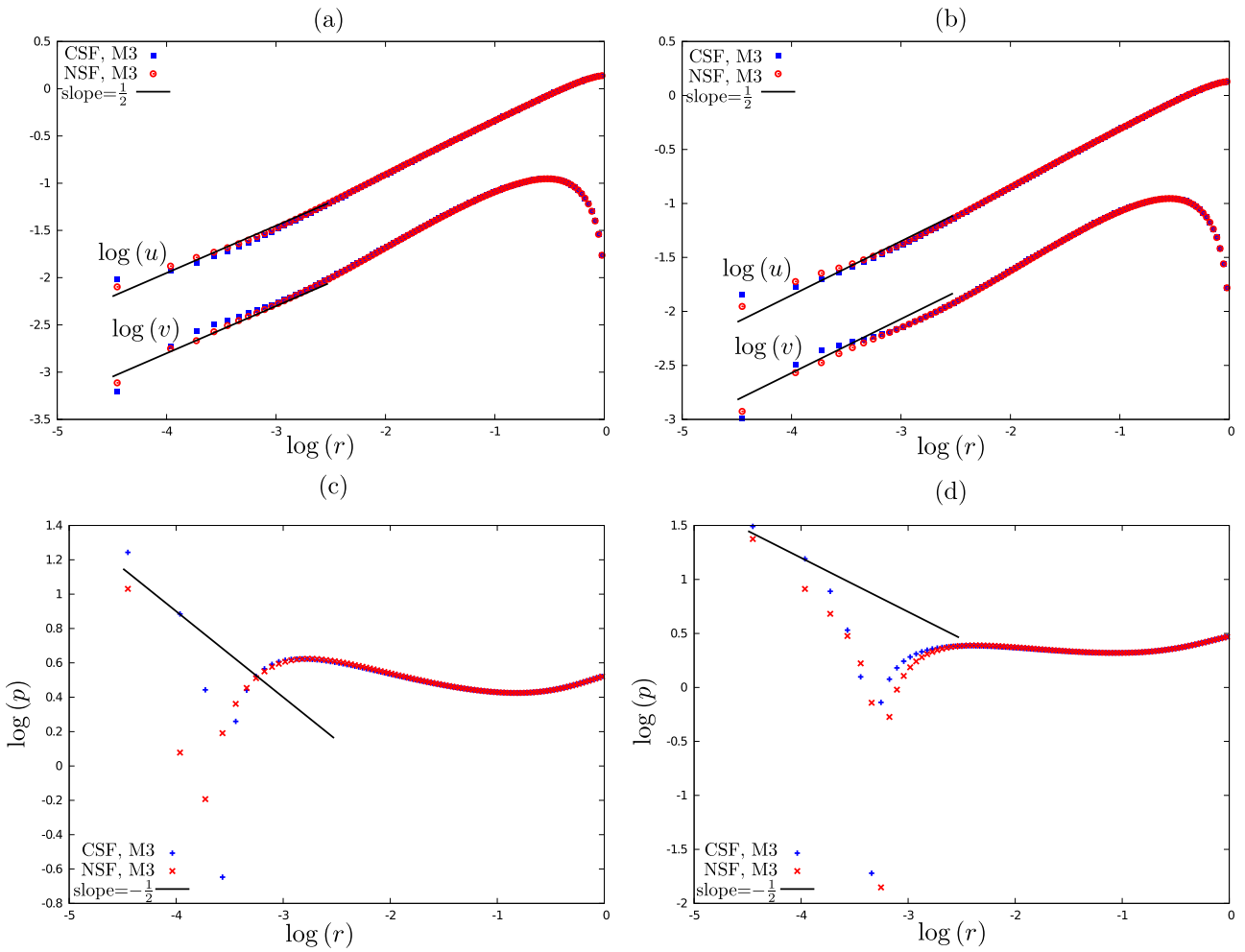


FIG. 18. Asymptotic variation near the stick-slip transition point of (a) u, v (PTT), (b) u, v (Giesekus), (c) p (PTT), and (d) p (Giesekus) along the line $\theta = 3\pi/4$ considering the half-length $L = 4$ with $\beta = 1/9$.

asymptotic results can be summarized as follows:

$$\begin{aligned} \lambda &\sim \begin{cases} r^{-\frac{15}{11}}, & \text{PTT}, \\ r^{-\frac{21}{16}}, & \text{Giesekus}, \end{cases} \quad \mu \sim \begin{cases} r^{-\frac{3}{22}}, & \text{PTT}, \\ r^0, & \text{Giesekus}, \end{cases} \\ \nu &\sim \begin{cases} r^{\frac{12}{11}}, & \text{PTT}, \\ r^{\frac{21}{16}}, & \text{Giesekus}. \end{cases} \end{aligned} \quad (4.3)$$

These behaviors predict that the solvent stress should dominate the polymer stress close to the singularity, which implies that the kinematics are Newtonian-like. The above behaviors are expected to hold on small radial distances and uniformly in angle, apart from near the stick and slip surfaces, where very thin cusplike boundary layers are present.

We consider first the parameter case $Wi = 1$, $\beta = 1/2$ and analyze the numerical results at the stick-slip transition point along the rays $\theta = \pi/2$ in Figs. 9 and 10 and $\theta = 3\pi/4$ in Figs. 11 and 12; these angles being illustrated in Fig. 8. Figure 9 presents the verification of the singularity behavior for the velocity components and the pressure, while Figs. 10(a) and 10(b) describe the results for the polymer Cartesian extra-stress components. Also included are results for the NS variables in Figs. 10(c) and 10(d). Figure 9 shows that the CSF and NSF produce similar results in capturing the expected asymptotic behaviors for the velocity and pressure fields. However, for the Cartesian components of the extra-stress tensor depicted in Figs. 10(a) and 10(b), it is evident that meshes M1 and M2 in both formulations are too coarse to capture the required behavior for either fluid model. In particular, CSF struggles with the T_{22} component, which clearly needs a finer mesh and appears to converge slower to its asymptotics than the other two

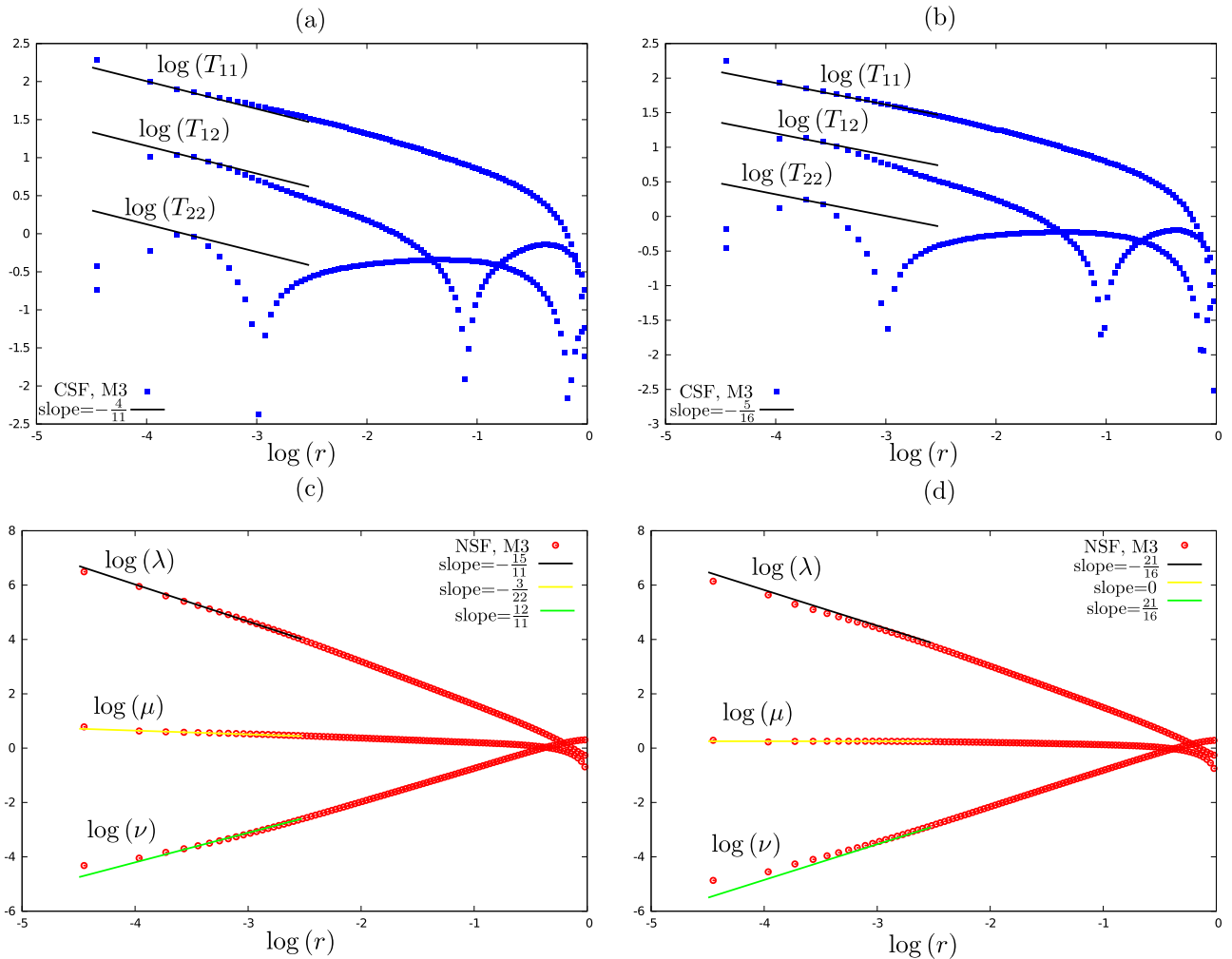


FIG. 19. Asymptotic variation near the stick-slip transition point of (a) T_{11} , T_{12} , T_{22} (PTT), (b) T_{11} , T_{12} , T_{22} (Giesekus), (c) λ , μ , ν (PTT), and (d) λ , μ , ν (Giesekus) along the line $\theta = 3\pi/4$ considering the half-length $L = 4$ with $\beta = 1/9$.

components. In contrast to the CSF, as illustrated in Figs. 10(c) and 10(d), the NSF produces results in very good agreement with (4.3) capturing accurately the theoretical behaviors. Although both formulations capture the required behaviors on the finer meshes M2

and M3, there are clear differences in rate of convergence for the different components. Noteworthy is the ability of the NSF to capture the NS behaviors even on the coarsest mesh M1. Similar behaviors are observed at $\theta = 3\pi/4$, as shown in Figs. 11 and 12. These results

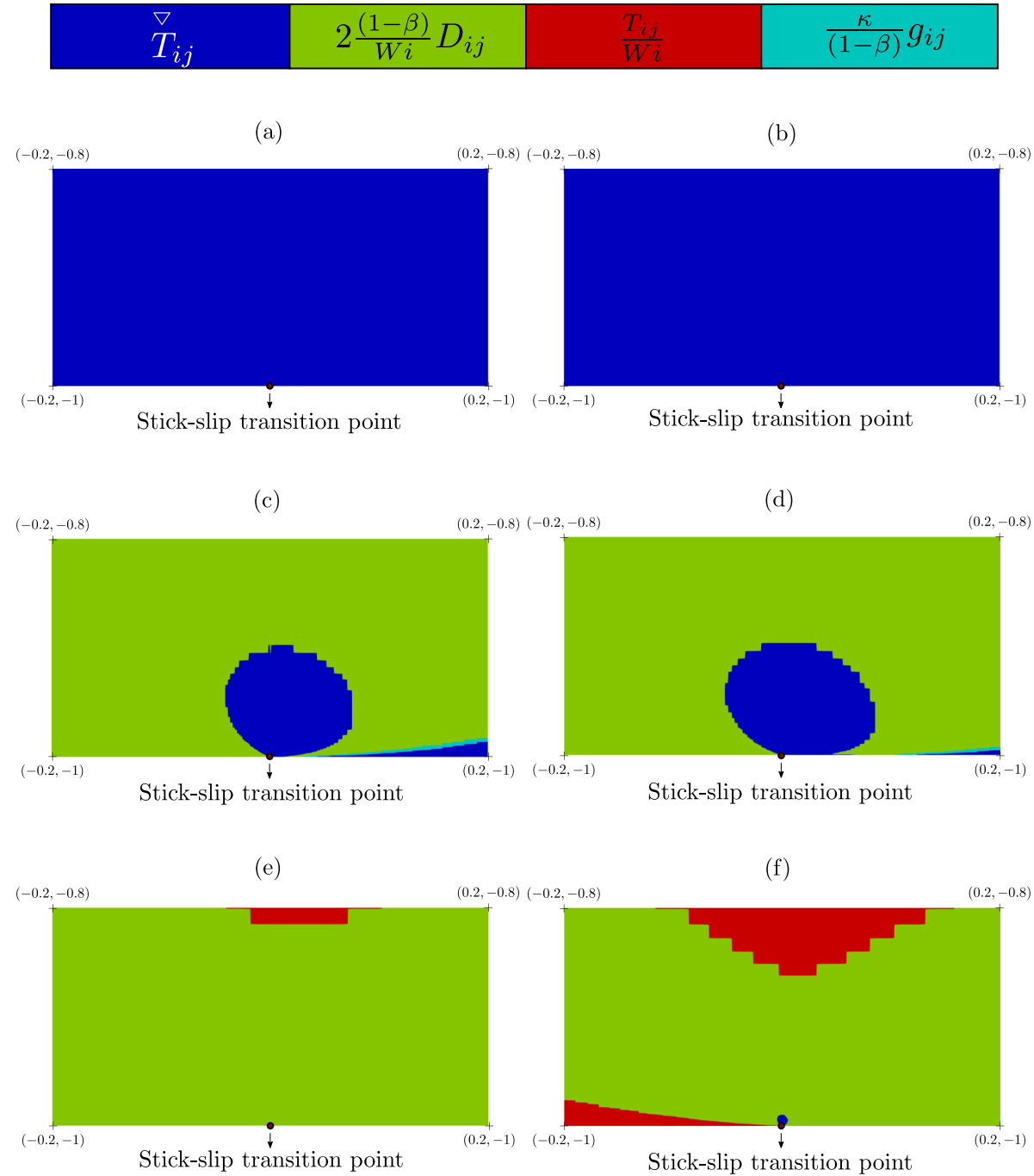


FIG. 20. Dominance of the groups of terms (4.12) for the components (a) $ij = 11$ (PTT), (b) $ij = 11$ (Giesekus), (c) $ij = 12$ (PTT), (d) $ij = 12$ (Giesekus), (e) $ij = 22$ (PTT), and (f) $ij = 22$ (Giesekus) within the Cartesian constitutive equation using $\beta = 1/9$ and $Wi = 1$.

emphasize that smaller length scales are needed for the Cartesian stresses to capture the singular behavior compared to the natural stress variables. We also remark that the Cartesian extra-stress values calculated using the NS variables through (2.25)–(2.27) do not show

a markedly significant improvement, in contrast to the re-entrant corner singularity.³⁴

The asymptotic solutions local to the singularity determined in Refs. 30, 31, and 29 for the stream function (adjusted here for the

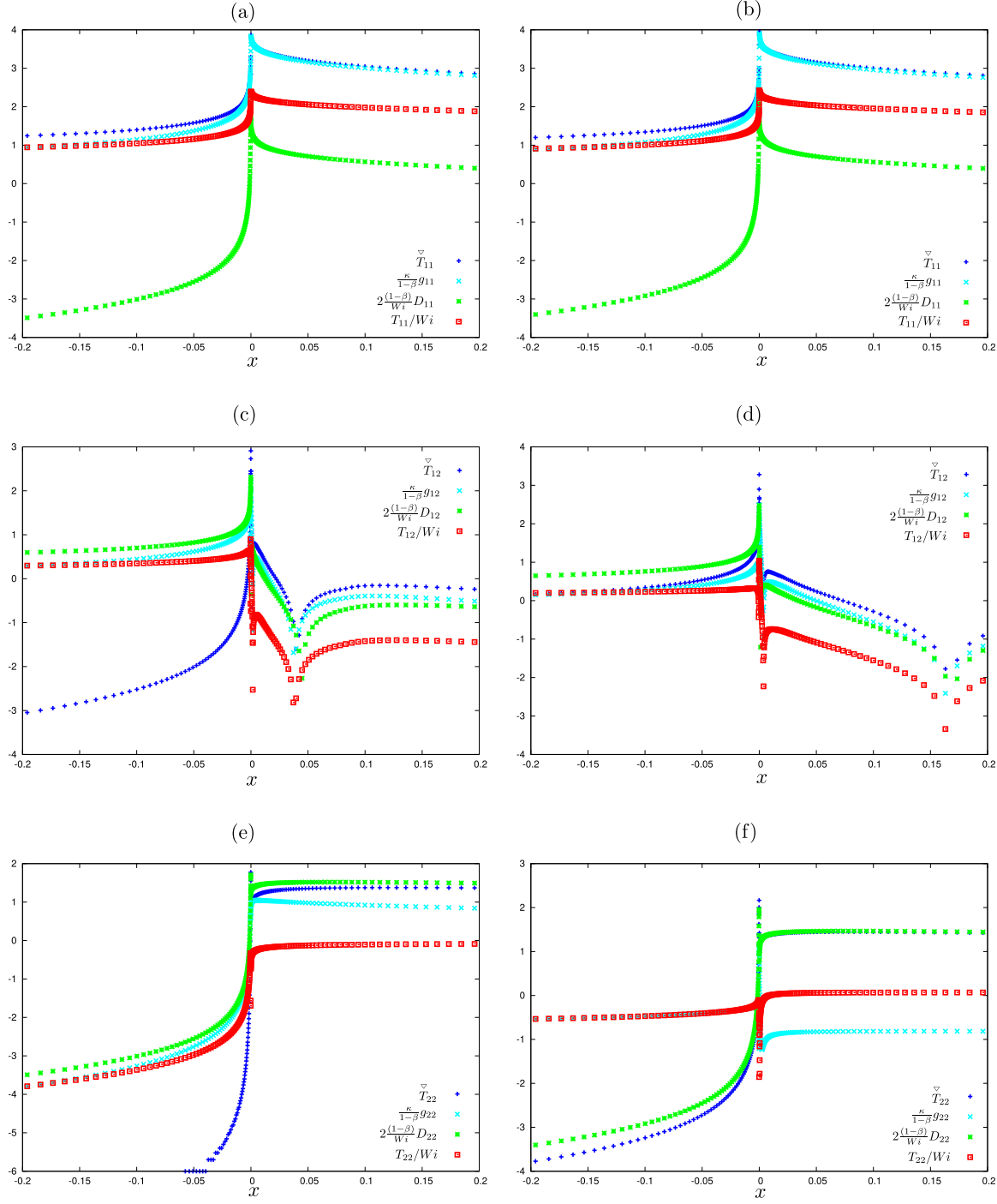


FIG. 21. Dominance of the groups of terms (4.12) for the components (a) $ij = 11$ (PTT), (b) $ij = 11$ (Giesekus), (c) $ij = 12$ (PTT), (d) $ij = 12$ (Giesekus), (e) $ij = 22$ (PTT), and (f) $ij = 22$ (Giesekus) within the Cartesian constitutive equation using $\beta = 1/9$ and $Wi = 1$.

current flow orientation) and natural stress variables are

$$\begin{aligned}\psi &\sim 2C_0 r^{\frac{3}{2}} \sin \theta \cos \frac{\theta}{2}, & \lambda &\sim \frac{C_1}{C_0} \left(\frac{\psi}{C_0} \right)^{n_1}, \\ \mu &\sim C_2 \left(\frac{\psi}{C_0} \right)^{n_2}, & \nu &\sim C_0^2 C_3 \left(\frac{\psi}{C_0} \right)^{n_3},\end{aligned}\quad (4.4)$$

where

$$\begin{aligned}\text{PTT: } n_1 &= -\frac{10}{11}, & n_2 &= -\frac{1}{11}, & n_3 &= \frac{8}{11}, \\ \text{Giesekus: } n_1 &= -\frac{7}{8}, & n_2 &= 0, & n_3 &= \frac{7}{8}.\end{aligned}\quad (4.5)$$

Fitting these expressions to the NSF numerical solution, we may determine the four constants (C_0 , C_1 , C_2 , C_3), estimates (from the ray $\theta = \pi/2$) being recorded in Table II. For comparison, we also record the C_0 value in the Newtonian case, which agrees accurately with the analytical value reported in Ref. 6 of $(3/2\pi)^{1/2} \approx 0.691$. It is worth remarking that the numerical estimates for the constants along the ray $\theta = 3\pi/4$ give very similar values (agreeing to 1 d.p.) to those for $\theta = \pi/2$.

We now use these results to obtain estimates of the radial length scales on which the leading order Cartesian stress behaviors are expected to hold. The asymptotic behaviors (4.4) are predicated on the dominance of the solvent extra-stress $T^s = 2\beta D$ over the polymer extra-stress T , i.e.,

$$T \ll T^s \quad (4.6)$$

near the transition point, which should hold for nonzero β . Using the results in Refs. 29–31, we have that the polymer stress behaves as

$$T \sim \frac{(1-\beta)}{Wi} \lambda \mathbf{v} \mathbf{v}^T \quad \text{as } r \rightarrow 0, \quad (4.7)$$

where λ is recorded in (4.4). Since we are using local polar coordinates $x = r \cos \theta$, $y + 1 = r \sin \theta$, the stream function in (4.4) can be

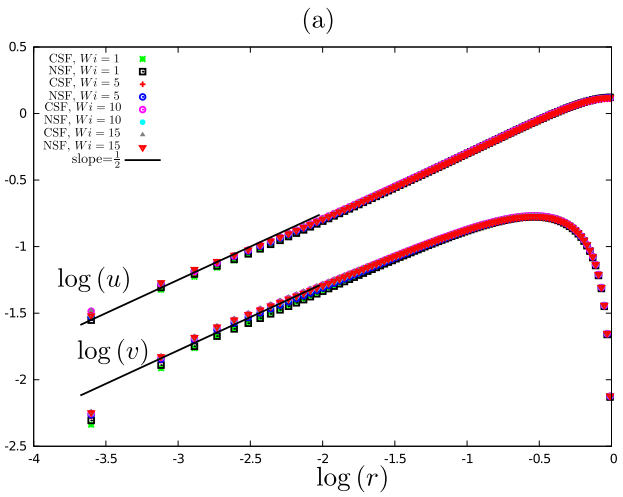


FIG. 22. Asymptotic variation near the stick-slip transition point of (a) u , v and (b) p along the line $\theta = \pi/2$ for PTT with $\beta = 1/2$. The Weissenberg numbers adopted were $Wi = 1, 5, 10, 15$.

written as

$$\psi = \sqrt{2} C_0 (y+1) \left((x^2 + (y+1)^2)^{\frac{1}{2}} + x \right)^{\frac{1}{2}}.$$

We can thus obtain expressions for the Cartesian velocity components and hence the solvent and polymer stresses, which are most conveniently written in polar coordinates as follows:

$$\begin{aligned}u &= C_0 r^{\frac{1}{2}} \cos \left(\frac{\theta}{2} \right) (3 - \cos \theta), & v &= -C_0 r^{\frac{1}{2}} \cos \left(\frac{\theta}{2} \right) \sin \theta, \\ T_{ij}^s &= \beta C_0 r^{-\frac{1}{2}} f_{ij}(\theta), & T_{ij} &= \frac{(1-\beta)}{Wi} C_1 r^{1+\frac{3}{2}n_1} h_{ij}(\theta),\end{aligned}$$

where

$$\begin{aligned}f_{11}(\theta) &= \cos \left(\frac{\theta}{2} \right) (2 \cos^2 \theta - \cos \theta + 1), \\ f_{12}(\theta) &= \sin \left(\frac{\theta}{2} \right) (2 \cos^2 \theta + \cos \theta + 1), \quad f_{22}(\theta) = -f_{11}(\theta),\end{aligned}\quad (4.8)$$

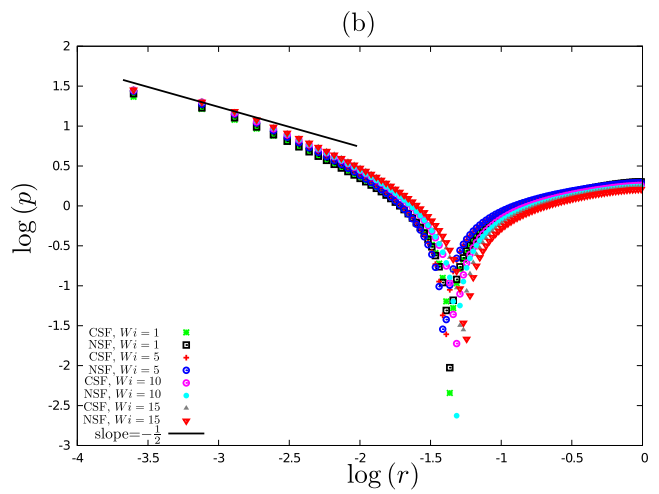
and

$$\begin{aligned}h_{11}(\theta) &= \left(2 \sin \theta \cos \left(\frac{\theta}{2} \right) \right)^{n_1} \cos^2 \left(\frac{\theta}{2} \right) (3 - \cos \theta)^2, \\ h_{12}(\theta) &= h_{11}(\theta) \frac{\sin \theta}{(3 - \cos \theta)}, \quad h_{22}(\theta) = h_{12}(\theta) \frac{\sin \theta}{(3 - \cos \theta)},\end{aligned}\quad (4.9)$$

with n_1 specified in (4.5). We may compare the absolute value of the corresponding solvent and polymer components to obtain the radial estimates

$$r_{ij} = \left| \frac{\beta Wi}{(1-\beta)} \frac{C_0}{C_1} \frac{f_{ij}(\theta)}{h_{ij}(\theta)} \right|^{\frac{2}{3(n_1+1)}}. \quad (4.10)$$

The functions $|f_{ij}(\theta)/h_{ij}(\theta)|$ are plotted in Fig. 13 and for uniform dominance of the solvent stress across the main interval of θ as



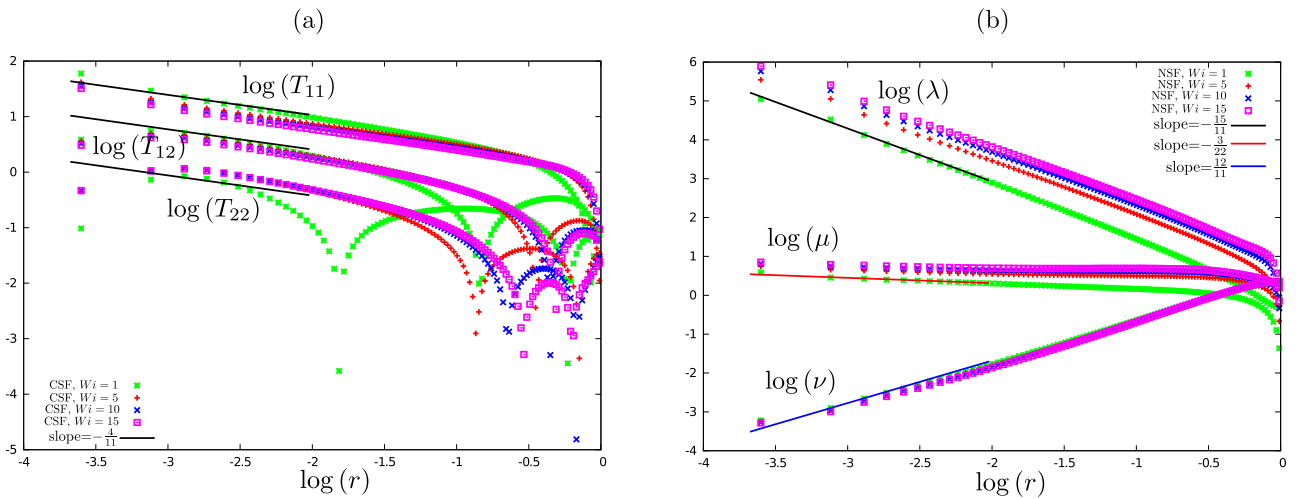


FIG. 23. Asymptotic variation near the stick-slip transition point of (a) T_{11} , T_{12} , T_{22} and (b) λ , μ , ν along the line $\theta = \pi/2$ for PTT with $\beta = 1/2$. The Weissenberg numbers adopted were $Wi = 1, 5, 10, 15$.

illustrated by dotted lines in Fig. 13, we require for the PTT and Giesekus models to use

$$\begin{aligned} \left| \frac{f_{11}}{h_{11}} \right| &= 0.21, & \left| \frac{f_{12}}{h_{12}} \right| &= \begin{cases} 0.64, & \text{PTT}, \\ 0.63, & \text{Giesekus}, \end{cases} \\ \left| \frac{f_{22}}{h_{22}} \right| &= \begin{cases} 1.73, & \text{PTT}, \\ 1.71, & \text{Giesekus}, \end{cases} \end{aligned} \quad (4.11)$$

which give the radial estimates recorded in the last three columns of Table II on using the estimates of the ratio C_0/C_1 . It is clear that the radial estimates from the 11 and 12 components show that substantially smaller meshes are needed before their solvent stress components dominate those of the polymer.

B. Numerical investigation of the boundary layers

Additional insights into the stick-slip stress singularity behavior may be gained by exploring the boundary layer structures. Here, we compare the absolute magnitude of the terms in the CSF of the constitutive equations. We thus record

$$\max\left(\left|\frac{\mathbf{T}_{ij}}{Wi}\right|, \left|\frac{\nabla \mathbf{T}_{ij}}{(1-\beta)}\right|, \left|\frac{\kappa}{(1-\beta)}\mathbf{g}_{ij}\right|, \left|\frac{2(1-\beta)}{Wi}\mathbf{D}_{ij}\right|\right) \quad (4.12)$$

for each of the three components $ij = 11, 12$, and 22 separately in Fig. 14 for the parameter case $\beta = 1/2$, $Wi = 1$, and $\kappa = 0.1$. In these figures, we have considered a small region local to the singularity and the maps are labeled without the presence of the modulus sign for convenience. Equations (2.9)–(2.11) give the explicit representation of the terms. These figures indicate the dominance of the upper convective polymer stress derivative (blue representation) near to the singularity but away from the stick and slip boundaries. According to the first row subplots of Fig. 14, it dominates uniformly. The subplots in the second and third rows of Fig. 14 indicate that the rate-of-strain terms (green representation) dominate at the stick surface with the demarcation with the upper convected

derivative terms being cusplike near to the singularity (transition point). This supports the presence of the stick surface boundary layer, where the rate-of-strain terms must be recovered for viscometric behavior. Similarly at the slip surface, it can be seen in the second row of Fig. 14 the dominance of the quadratic stress terms, as predicted theoretically for the slip boundary layer. These structures are apparent for both models. In order to clarify the threshold used to determine which term is dominant, we have also plotted in Fig. 15 the results of the four terms of (4.12) in the horizontal line $y \approx 1.999925$ (near to the singularity).

C. Numerical investigation for small solvent viscosities

Here, we examine the results for the smaller fractional viscosity ratio of $\beta = 1/9$. Due to the CFL stability restriction in the time step, to achieve numerical results on the finest mesh M3, we are limited spatially to considering a reduced domain, e.g., the dimensionless domain half-length is now taken as $L = 4$. Although the global results will not be accurate, it is worth noting that this truncated channel length does not change the numerical structure of the stress singularities near the stick-slip transition point, including the estimates of the constants presented in Table II. We base this statement on observing that the results for $\beta = 1/2$ in Sec. IV A did not change when $L = 8$ was reduced to $L = 4$.

TABLE III. Estimate values of C_0 , C_1 , C_2 , and C_3 as well as radial distances (4.10) for the PTT model with $\kappa = 0.1$ and fractional viscosity $\beta = 1/2$.

Wi	C_0	C_1	C_2	C_3	r_{11}	r_{12}	r_{22}
1	0.748	1.19	1.18	3.86	3.53×10^{-7}	1.23×10^{-3}	1.84
5	0.775	4.70	2.07	3.18	2.58×10^{-6}	9.04×10^{-3}	1.34
10	0.783	8.15	2.59	2.93	7.93×10^{-6}	2.77×10^{-2}	41.36
15	0.788	11.19	2.96	2.79	1.59×10^{-5}	5.56×10^{-2}	82.91

Figures 16 and 17 reproduce the results of Figs. 9 and 10, but for the case $\beta = 1/9$. While the velocity and extra-stresses (both Cartesian and natural) illustrate convergence to the theoretical behaviors, the pressure does not suggest the need for a more refined mesh for this

variable. However, the falloff in the Cartesian components T_{12} and T_{22} for the closest points is noteworthy for both models and reminiscent of behavior at the re-entrant corner singularity in contraction flow (see, for example, Ref. 48). The radial distance estimates (4.10)

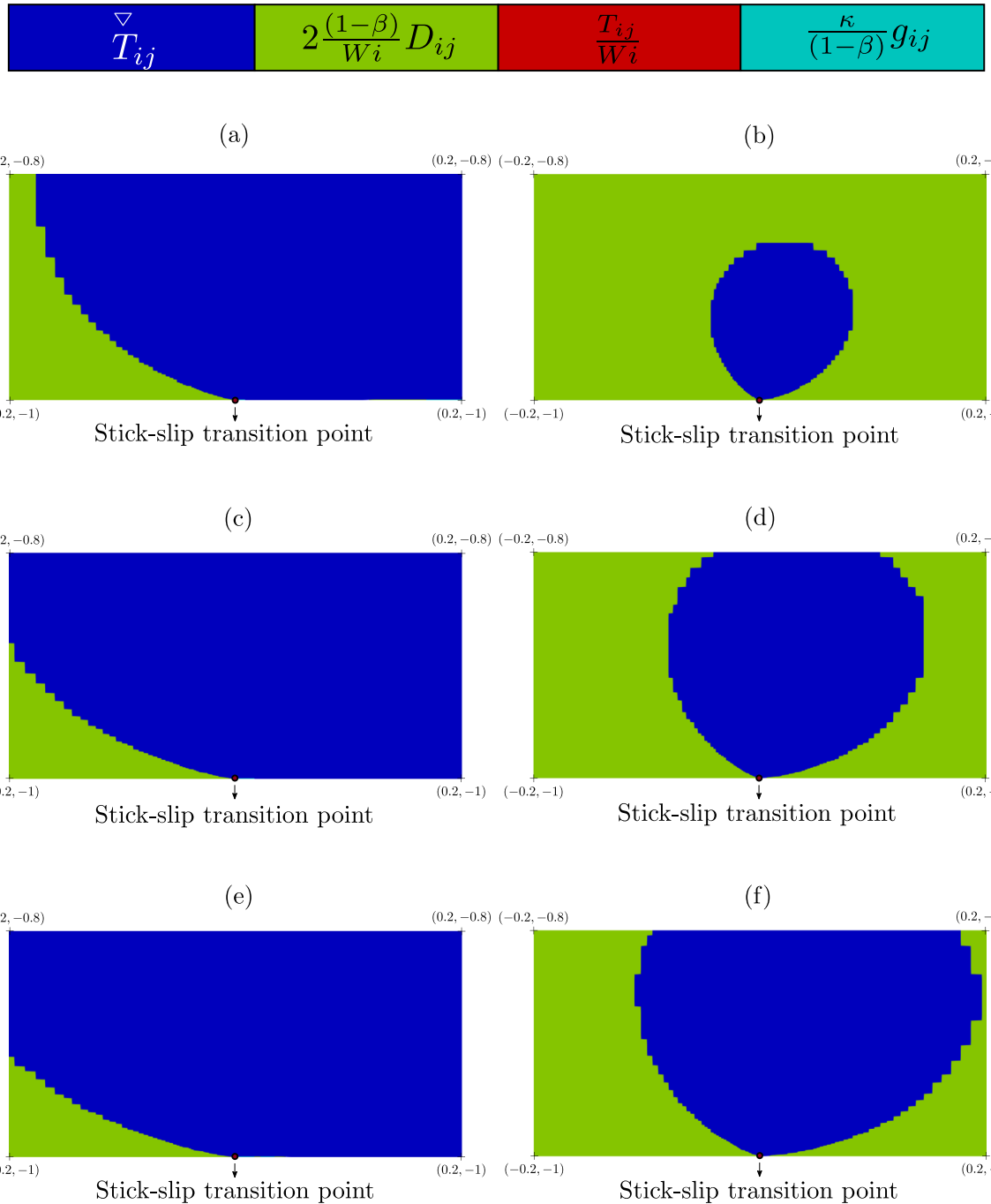


FIG. 24. Dominance of the groups of terms (4.12) for components 12 and 22 within the Cartesian constitutive equation for PTT with $\beta = 1/2$: first row for $Wi = 5$ and components (a) $ij = 12$ and (b) $ij = 22$, second row for $Wi = 10$ and components (c) $ij = 12$ and (d) $ij = 22$, and third row for $Wi = 15$ and components (e) $ij = 12$ and (f) $ij = 22$.

have now reduced significantly for this fractional viscosity and are recorded in Table II. This is mainly due to the effect of the power of β in the expressions, the power being $7\frac{1}{3}$ for PTT and $5\frac{1}{3}$ for Giesekus (the constants C_0 , C_1 are relatively insensitive to changes in β).

It also highlights the extreme challenge that numerical schemes face in capturing the singularity for small solvent viscosities (and in fact the emergence of another, as yet theoretically unknown singularity as the solvent viscosity vanishes in the limit $\beta \rightarrow 0$).

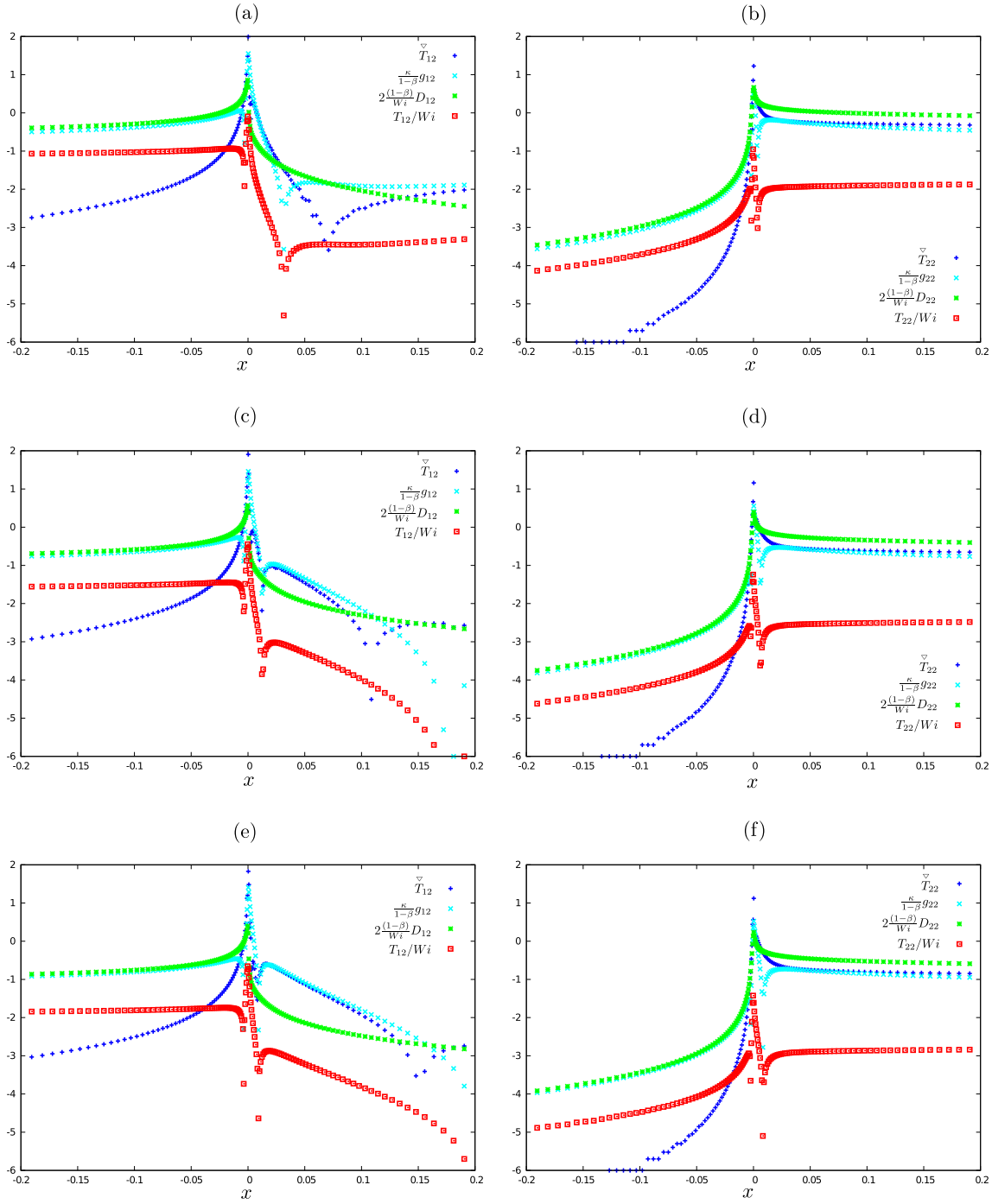


FIG. 25. Dominance of the groups of terms (4.12) for components 12 and 22 within the Cartesian constitutive equation for PTT with $\beta = 1/2$: first row for $Wi = 5$ and components (a) $j = 12$ and (b) $j = 22$, second row for $Wi = 10$ and components (c) $j = 12$ and (d) $j = 22$, and third row for $Wi = 15$ and components (e) $j = 12$ and (f) $j = 22$.

The plots for the velocities and extra-stresses confirm no significant variations in the predicted slopes from the theoretical ones, confirming the insensitivity of the power-law exponents in (4.4) to the solvent fraction. Results for $\beta = 1/9$ along the ray $\theta = \frac{3\pi}{4}$ are also presented in Figs. 18 and 19.

The Cartesian boundary layer plots in Fig. 20 emphasize the shrinking dominance of the upper-conveyed stress derivative near to the singularity and hence the relevance of the stretching solution (4.7). For the PTT 22 component, it is no longer visible. Evidence of cusplike boundary layers at both the stick and slip surfaces is still apparent in the 12 component plots. Additionally, we have also shown in Fig. 21, the profiles of the four terms of (4.12) along the horizontal line $y \approx 1.999\,925$.

D. Influence of the Weissenberg number

In this section, we numerically show that the stick-slip singularity is independent of the Weissenberg number, varying this number as 5, 10, and 15. In order to save CPU time and maintain numerical stability, we use the intermediate mesh M2 (see Table I), truncated domain length $L = 8$ and solvent fraction $\beta = 1/2$. We emphasize that the dimensionless domain half-length adopted here does not influence the numerical results captured in the vicinity of the singularity, as shown by the results in Appendix B.

Figures 22 and 23 confirm that the leading order asymptotic behaviors of the variables are independent of the selected Weissenberg numbers. For the velocity and pressure behaviors in Fig. 22, the CSF and NSF produce very similar results. The extra-stress components of the CSF are shown in Fig. 23(a), while the natural stress variables are given in Fig. 23(b). It is noteworthy that increasing Wi leads to improvement in the slope results for the T_{22} component in the CSF.

The influence of the Weissenberg number on the analytical constants (C_0, C_1, C_2, C_3) [see Eq. (4.4)] from the ray $\theta = \pi/2$ is described in Table III. Results for the dominance of the terms for PTT with selected Wi are shown in Fig. 24, with only the 12 and 22 components plotted, since there being no change for the 11 component to that seen in Fig. 14(a) for $Wi = 1$. The maps illustrate the growing dominance of the upper convected stress derivative term as the Weissenberg number is increased, with Table III showing increasing radial distances on which the singularity is anticipated to be found. A profile investigation is also presented in Fig. 25 to quantify the dominance of the terms on the boundary layer structures.

V. DISCUSSION

A finite-difference numerical scheme using a semiexplicit projection method has been implemented to address the planar stick-slip flow for the PTT and Giesekus viscoelastic models. The scheme solves the transient problem and has been applied to two different formulations of the polymer constitutive equations, the traditional formulation using Cartesian stresses (CSF) and the other using natural stresses (NSF). The Cartesian stress formulation uses a fixed basis for the polymer stress, while the natural stress formulation aligns the polymer extra-stress along particle paths/streamlines.

The purpose of this investigation was to understand the efficacy of both formulations in a flow problem with a challenging singularity present. The main conclusion of the numerical tests in Sec. III is the significant improvement in the rate of convergence both temporally for the extra-stress residuals and spatially in capturing the stress singularity behavior that the NSF affords over the CSF. In addition, as presented in Sec. IV, the NSF results allow consistent estimates of the constants in the asymptotic behaviors (4.4), which in turn can be used to derive theoretical estimates in Table II of the length scales on which the solvent stress dominates the polymer stress near to the singularity. For $\beta = 1/2$, these suggest radial distances of 10^{-6} for PTT and 10^{-5} for Giesekus, where the pressure and Cartesian T_{22} component are the slowest convergent variables and only just beginning to attain their singular behaviors on the finest mesh M3. The situation is starkly different for the smaller fractional viscosity case of $\beta = 1/9$. While the natural stress variables capture their singular behaviors, the Cartesian components clearly struggle even on the finest mesh M3. The radial estimates r_{ij} described in Table II have now reduced considerably, illustrating the severe challenge capturing the singularity possessed to the Cartesian formulation for small solvent viscosity. It is on these radial distances that the theoretical asymptotic structure at the singularity presented in Refs. 30 and 31 is expected to be found. However, numerical evidence of the structure is still apparent on larger length scales, as evidenced in the dominance plots for each group of terms in the component equations of the Cartesian form of the polymer constitutive equations. As is often the case, and apparent here, the asymptotic results can hold on scales larger than their strict mathematical region of validity.

ACKNOWLEDGMENTS

The authors would like to thank the financial support from SPRINT/FAPESP (Grant No. 2018/22242-0). C. M. Oishi acknowledges CNPq (Conselho Nacional de Desenvolvimento Científico e Tecnológico; Grant No. 307459/2016-0) and FAPESP (Fundação de Amparo à Pesquisa do Estado de São Paulo; Grant No. 2013/07375-0). I. L. Palhares Junior acknowledges the financial support from FAPESP (Grant No. 2014/17348-2) and BEPE (Grant No. 2016/20389-8).

APPENDIX A: VERIFICATION FOR NEWTONIAN FLOW

We first verify the scheme for Newtonian flow, where the contribution of the non-Newtonian effects is neglected. Thus, only step 1 of the algorithm is applied. The u velocity component along the free surface in Newtonian flow is given by the expression⁵⁰

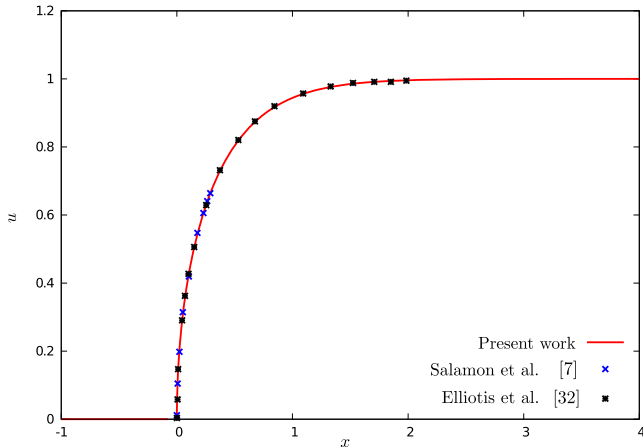
$$u(x) = 2a_{\frac{1}{2}}x^{\frac{1}{2}} - 2a_{\frac{3}{2}}x^{\frac{3}{2}} + 2a_{\frac{5}{2}}x^{\frac{5}{2}} + O(x^{\frac{7}{2}}), \quad \text{as } x \rightarrow 0, \quad (\text{A1})$$

TABLE IV. Set of values for x and u used to calculate the coefficients $a_{1/2}$, $a_{3/2}$, and $a_{5/2}$.

Values			
x	0.102 512	0.499 067	0.888 449
u	0.425 169 5	0.803 605 3	0.926 177 8

TABLE V. Coefficients of the expansion (A1) near to the singularity for the Newtonian stick-slip flow.

References	$a_{1/2}$	$a_{3/2}$	$a_{5/2}$
Present work (M2)	0.691 25	0.271 54	0.052 32
Karapetsas (M11, $h_{min} = 7.0e - 06$) ³⁸	0.691 57	0.271 97	0.052 47
Tanner and Huang (analytical sol.) ⁶	0.690 99
Salamon <i>et al.</i> ⁷	0.691 60	0.271 83	0.052 32
Elliottis <i>et al.</i> ⁵¹	0.690 99	0.264 50	0.030 37

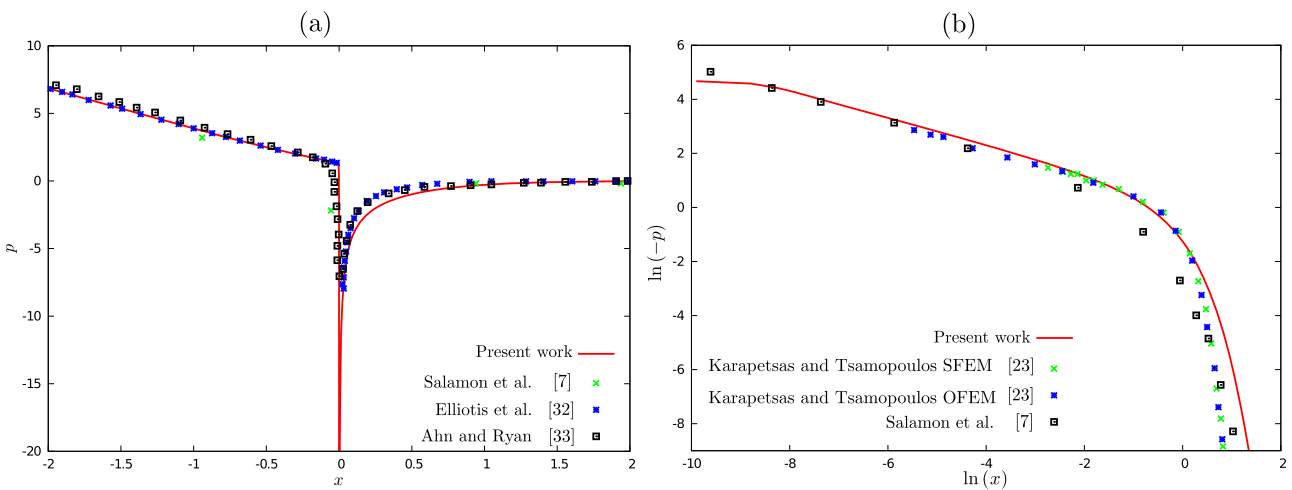
**FIG. 26.** Comparison results for the velocity along the horizontal line $y = 1$.

near to singularity. This equation, together with the values in [Table IV](#), may be used to calculate the coefficients $a_{1/2}$, $a_{3/2}$ and $a_{5/2}$ shown in [Table V](#). In this section, we have considered the intermediate mesh M2, as defined in [Table I](#).

First, as given in [Table V](#), our results compare well with those of the literature. In addition, we have plotted the horizontal velocity component u and the pressure p calculated along the stick-slip surface $y = 1$, as presented, respectively, in [Figs. 26](#) and [27\(a\)](#). [Figure 27\(b\)](#) is presented as an additional comparison. According to these figures, we can confirm that our results are in good agreement with the numerical results presented by the literature.^{7,38,49,51}

APPENDIX B: EFFECT OF THE TRUNCATION LENGTH FOR THE STRESS SINGULARITY RESULTS

We examine here the effect of the domain truncation length for capturing the numerical results in the vicinity of the stick-slip transition point. For this purpose, we have considered the PTT model on the M2 mesh and three different dimensionless domain half-lengths $L = 4, 8, 16$, varying the Weissenberg number as 1, 5, 10, and 15. According to [Figs. 28](#) and [29](#), we can confirm that the results for the velocity and pressure fields are very similar for all three truncation lengths. Moreover, it is relevant to highlight that the numerical results for the extra-stress tensor and for natural stress variables presented in [Figs. 30](#) and [31](#) are also very similar for $L = 4, 8, 16$, even for large Wi . Therefore, the dimensionless domain half-lengths adopted in our study do not influence the numerical results captured in the vicinity of the singularity.

**FIG. 27.** Comparison results for the pressure (a) and results for $\ln(-p)$ and $\ln(x)$ (b) along the horizontal line $y = 1$.

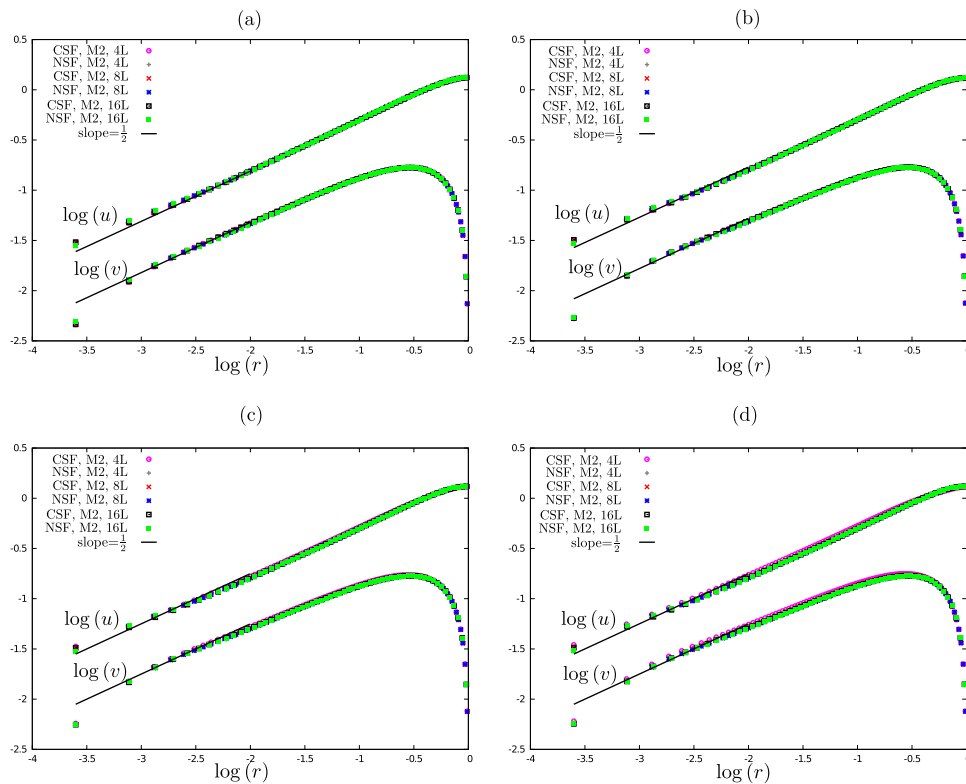


FIG. 28. Asymptotic variation near the stick-slip transition point of u and v along the line $\theta = \pi/2$ for different values of Wi : (a) $Wi = 1$, (b) $Wi = 5$, (c) $Wi = 10$, and (d) $Wi = 15$.

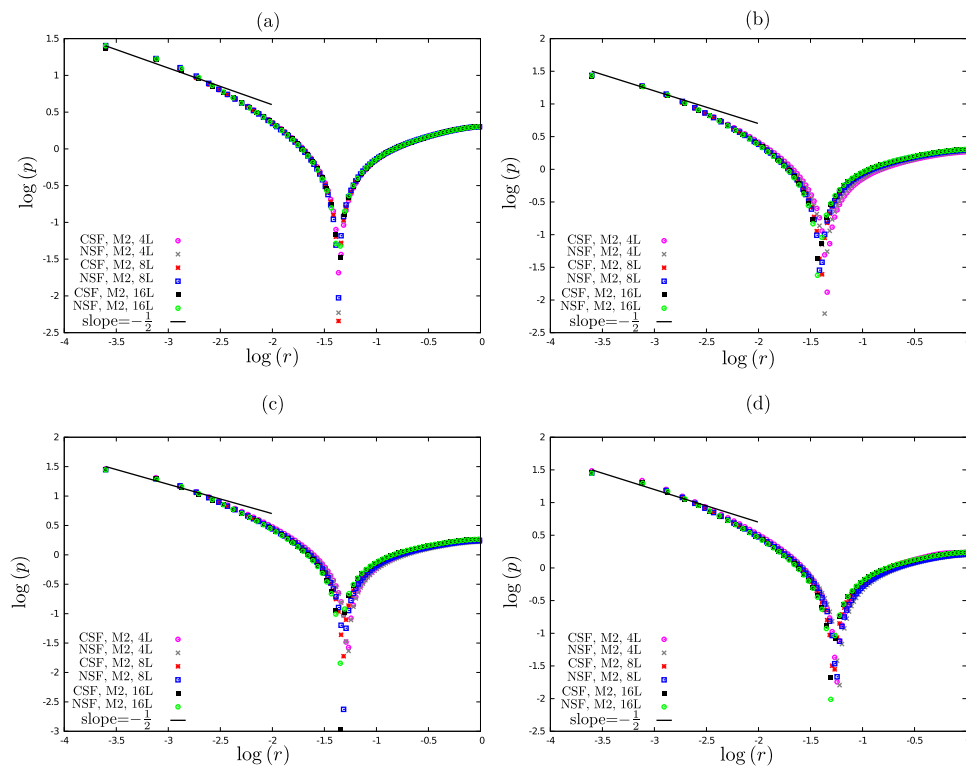


FIG. 29. Asymptotic variation near the stick-slip transition point of p along the line $\theta = \pi/2$ for different values of Wi : (a) $Wi = 1$, (b) $Wi = 5$, (c) $Wi = 10$, and (d) $Wi = 15$.

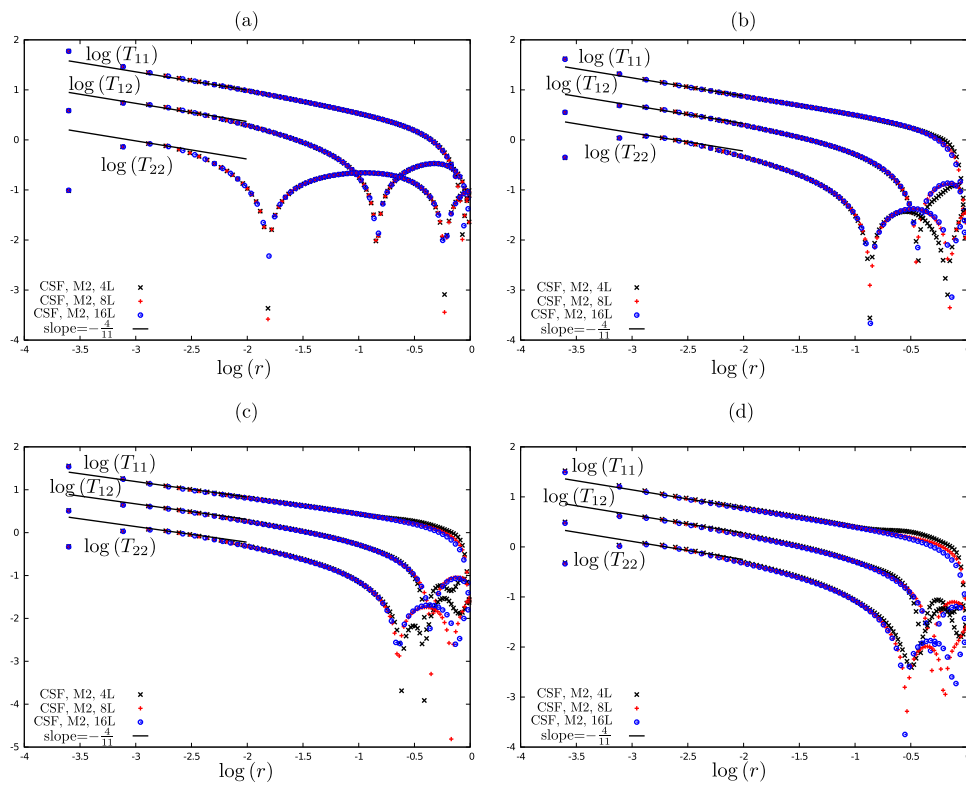


FIG. 30. Asymptotic variation near the stick-slip transition point of T_{11} , T_{12} , T_{22} , λ , μ , and ν along the line $\theta = \pi/2$ for different values of Wi : (a) $Wi = 1$, (b) $Wi = 5$, (c) $Wi = 10$, and (d) $Wi = 15$.

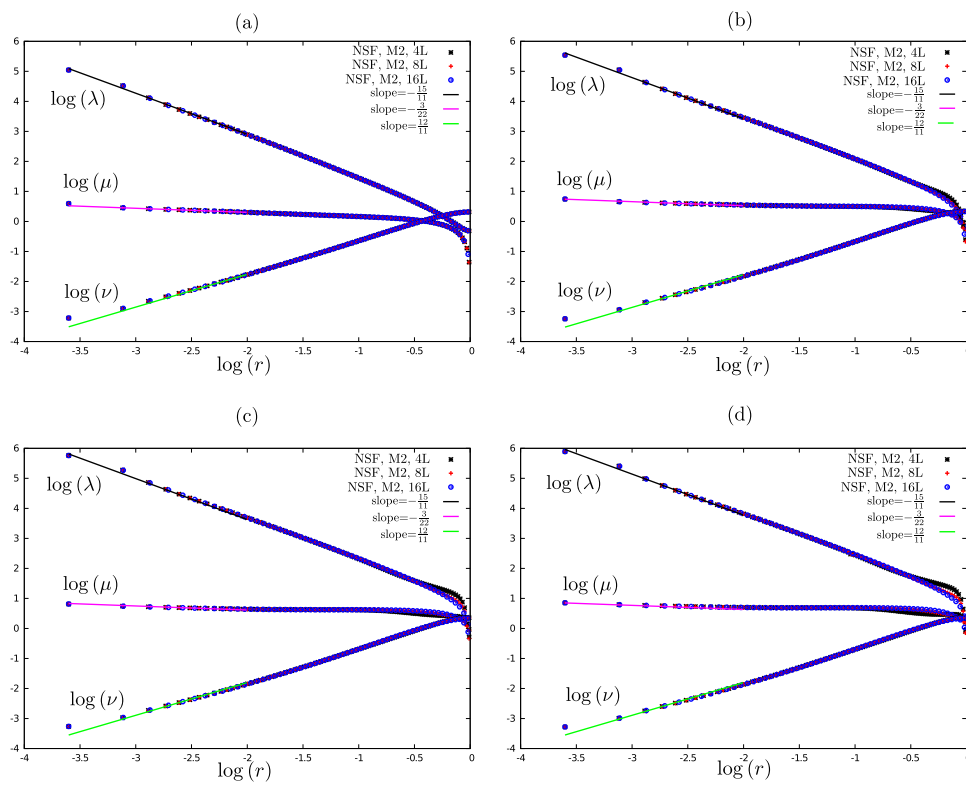


FIG. 31. Asymptotic variation near the stick-slip transition point of λ , μ , and ν along the line $\theta = \pi/2$ for different values of Wi : (a) $Wi = 1$, (b) $Wi = 5$, (c) $Wi = 10$, and (d) $Wi = 15$.

REFERENCES

- ¹J. R. A. Pearson, *Mechanics of Polymer Processing—Application to Polymer Processing (Videorecording)* (Center for Advanced Engineering Study, M.I.T., Cambridge, MA, 1974).
- ²R. I. Tanner, *Engineering Rheology*, The Oxford Engineering Science Series (Clarendon Press, 1985).
- ³S. Richardson, “A ‘stick-slip’ problem related to the motion of a free jet at low Reynolds numbers,” *Math. Proc. Cambridge Philos. Soc.* **67**, 477–489 (1970).
- ⁴S. Richardson, “The die swell phenomenon,” *Rheol. Acta* **9**(2), 193–199 (1970).
- ⁵S. A. Trogdon and D. D. Joseph, “The stick-slip problem for a round jet,” *Rheol. Acta* **19**(4), 404–420 (1980).
- ⁶R. I. Tanner and X. Huang, “Stress singularities in non-Newtonian stick-slip and edge flows,” *J. Non-Newtonian Fluid Mech.* **50**(2), 135–160 (1993).
- ⁷T. R. Salamon, D. E. Bornside, R. C. Armstrong, and R. A. Brown, “The role of surface tension in the dominant balance in the die swell singularity,” *Phys. Fluids* **7**(10), 2328–2344 (1995).
- ⁸C. J. S. Petrie and M. M. Denn, “Instabilities in polymer processing,” *AIChE J.* **22**(2), 209–236 (1976).
- ⁹M. M. Denn, “Issues in viscoelastic fluid mechanics,” *Annu. Rev. Fluid Mech.* **22**(1), 13–32 (1990).
- ¹⁰M. M. Denn, “Extrusion instabilities and wall slip,” *Annu. Rev. Fluid Mech.* **33**(1), 265–287 (2001).
- ¹¹R. G. Larson, “Instabilities in viscoelastic flows,” *Rheol. Acta* **31**(3), 213–263 (1992).
- ¹²M. D. Graham, “The sharkskin instability of polymer melt flows,” *Chaos* **9**(1), 154–163 (1999).
- ¹³Y. Kwon, “Numerical modelling of two-dimensional melt fracture instability in viscoelastic flow,” *J. Fluid Mech.* **855**, 595–615 (2018).
- ¹⁴O. Hassager, “Working group on numerical techniques,” in *Proceedings of the Vth Workshop on Numerical Methods in Non-Newtonian Flow* [J. Non-Newtonian Fluid Mech. **29**, 2–5 (1988)].
- ¹⁵M. Renardy, *Mathematical Analysis of Viscoelastic Flows* (Society for Industrial and Applied Mathematics, SIAM, Philadelphia, 2000).
- ¹⁶N. Phan-Thien and R. I. Tanner, “A new constitutive equation derived from network theory,” *J. Non-Newtonian Fluid Mech.* **2**(4), 353–365 (1977).
- ¹⁷N. Phan-Thien, “A nonlinear network viscoelastic model,” *J. Rheol.* **22**(3), 259–283 (1978).
- ¹⁸H. Giesekus, “A unified approach to a variety of constitutive models for polymer fluids based on the concept of configuration-dependent molecular mobility,” *Rheol. Acta* **21**(4), 366–375 (1982).
- ¹⁹R. B. Bird, R. C. Armstrong, and O. Hassager, *Dynamics of Polymeric Liquids*, Fluid Mechanics Vol. 1 (Wiley, New York, 1987).
- ²⁰L. L. Ferrás, A. M. Afonso, J. M. Nóbrega, and F. T. Pinho, “A numerical and theoretical study on viscoelastic fluid slip flows,” *Phys. Fluids* **29**(5), 053102 (2017).
- ²¹L. Campo-Deaño, R. P. A. Dullens, D. G. A. L. Aarts, F. T. Pinho, and M. S. N. Oliveira, “Viscoelasticity of blood and viscoelastic blood analogues for use in poly-dimethylsiloxane *in vitro* models of the circulatory system,” *Biomicrofluidics* **7**(3), 034102 (2013).
- ²²A. Ramiar, M. M. Larimi, and A. A. Ranjbar, “Investigation of blood flow rheology using second-grade viscoelastic model (Phan-Thien-Tanner) within carotid artery,” *Acta Bioeng. Biomed.* **19**(3), 27–41 (2017).
- ²³N. A. Talib and Ö. Ertunç, “Application of Giesekus model for capillary extrusion of rubber compound,” *J. Chem. Eng. Jpn.* **52**(2), 185–193 (2019).
- ²⁴D. Tang, F. H. Marchesini, D. R. D’hooge, and L. Cardon, “Isothermal flow of neat polypropylene through a slit die and its die swell: Bridging experiments and 3D numerical simulations,” *J. Non-Newtonian Fluid Mech.* **266**, 33–45 (2019).
- ²⁵Z. Khan, R. A. Shah, S. Islam, B. Jan, M. Imran, and F. Tahir, “Steady flow and heat transfer analysis of Phan-Thein-Tanner fluid in double-layer optical fiber coating analysis with slip conditions,” *Sci. Rep.* **6**, 34593 (2016).
- ²⁶A. Syrakos, Y. Dimakopoulos, and J. Tsamopoulos, “Theoretical study of the flow in a fluid damper containing high viscosity silicone oil: Effects of shear-thinning and viscoelasticity,” *Phys. Fluids* **30**(3), 030708 (2018).
- ²⁷L. L. Ferrás, A. M. Afonso, M. A. Alves, J. M. Nóbrega, and F. T. Pinho, “Electro-osmotic and pressure-driven flow of viscoelastic fluids in microchannels: Analytical and semi-analytical solutions,” *Phys. Fluids* **28**(9), 093102 (2016).
- ²⁸H. S. Gaikwad, P. Baghel, R. Sarma, and P. K. Mondal, “Transport of neutral solutes in a viscoelastic solvent through a porous microchannel,” *Phys. Fluids* **31**(2), 022006 (2019).
- ²⁹J. Evans, I. L. Palhares Junior, and C. M. Oishi, “Stresses of the Oldroyd-B, PTT and Giesekus fluids in a Newtonian velocity field near the stick-slip singularity,” *Phys. Fluids* **29**, 121604 (2017).
- ³⁰J. Evans, “Stick-slip and slip-stick singularities of the Phan-Thien-Tanner fluid,” *J. Non-Newtonian Fluid Mech.* **199**, 12–19 (2013).
- ³¹J. Evans, “Stick-slip singularity of the Giesekus fluid,” *J. Non-Newtonian Fluid Mech.* **222**, 24–33 (2015).
- ³²M. Renardy, “How to integrate the upper convected Maxwell (UCM) stresses near a singularity (and maybe elsewhere, too),” *J. Non-Newtonian Fluid Mech.* **52**(1), 91–95 (1994).
- ³³J. D. Evans and C. M. Oishi, “Transient computations using the natural stress formulation for solving sharp corner flows,” *J. Non-Newtonian Fluid Mech.* **249**, 48–52 (2017).
- ³⁴J. D. Evans, H. L. Franca, and C. M. Oishi, “Application of the natural stress formulation for solving unsteady viscoelastic contraction flows,” *J. Comput. Phys.* **388**(1), 462–489 (2019).
- ³⁵A. Fortin, A. Zine, and J.-F. Agassant, “Computing viscoelastic fluid flow problems at low cost,” *J. Non-Newtonian Fluid Mech.* **45**(2), 209–229 (1992).
- ³⁶F. P. T. Baaijens, “Application of low-order discontinuous Galerkin methods to the analysis of viscoelastic flows,” *J. Non-Newtonian Fluid Mech.* **52**, 37–57 (1994).
- ³⁷S.-C. Xue, R. I. Tanner, and N. Phan-Thien, “Three-dimensional numerical simulations of viscoelastic flows—predictability and accuracy,” *Comput. Methods Appl. Mech. Eng.* **180**, 305–331 (1999).
- ³⁸G. Karapetsas and J. Tsamopoulos, “On the stick-slip flow from slit and cylindrical dies of a Phan-Thien and Tanner fluid model. I. Steady state,” *Phys. Fluids* **21**(12), 123101 (2009).
- ³⁹M. Renardy, “The high Weissenberg number limit of the UCM model and the Euler equations,” *J. Non-Newtonian Fluid Mech.* **69**(2), 293–301 (1997).
- ⁴⁰P. Wapperom and M. Renardy, “Numerical prediction of the boundary layers in the flow around a cylinder using a fixed velocity field,” *J. Non-Newtonian Fluid Mech.* **125**(1), 35–48 (2005).
- ⁴¹M. I. Gerritsma and T. N. Phillips, “On the characteristics and compatibility equations for the UCM model fluid,” *Z. Angew. Math. Mech.* **88**(7), 523–539 (2008).
- ⁴²M. I. Gerritsma and T. N. Phillips, “On the use of characteristic variables in viscoelastic flow problems,” *IMA J. Appl. Math.* **66**(2), 127–147 (2001).
- ⁴³C. M. Oishi, F. P. Martins, M. F. Tome, J. A. Cuminato, and S. McKee, “Numerical solution of the eXtended Pom-Pom model for viscoelastic free surface flows,” *J. Non-Newtonian Fluid Mech.* **166**(3), 165–179 (2011).
- ⁴⁴A. J. Chorin and J. E. Marsden, *A Mathematical Introduction to Fluid Mechanics* (Springer, 1990), Vol. 3.
- ⁴⁵D. L. Brown, R. Cortez, and M. L. Minion, “Accurate projection methods for the incompressible Navier-Stokes equations,” *J. Comput. Phys.* **168**(2), 464–499 (2001).
- ⁴⁶F. S. Sousa, C. M. Oishi, and G. C. Buscaglia, “Spurious transients of projection methods in microflow simulations,” *Comput. Methods Appl. Mech. Eng.* **285**, 659–693 (2015).
- ⁴⁷G. Tryggvason, R. Scardovelli, and S. Zaleski, *Direct Numerical Simulations of Gas-Liquid Multiphase Flows* (Cambridge University Press, 2011).

⁴⁸M. A. Alves, F. T. Pinho, and P. J. Oliveira, "Benchmark solutions for the flow of Oldroyd-B and PTT fluids in planar contractions," *J. Non-Newtonian Fluid Mech.* **110**, 45–75 (2003).

⁴⁹Y.-C. Ahn and M. E. Ryan, "A finite difference analysis of the extrudate swell problem," *Int. J. Numer. Methods Fluids* **13**(10), 1289–1310 (1991).

⁵⁰H. K. Moffatt, "Viscous and resistive eddies near a sharp corner," *J. Fluid Mech.* **18**(1), 1–18 (1964).

⁵¹M. Elliotis, G. Georgiou, and C. Xenophontos, "Solution of the planar Newtonian stick-slip problem with the singular function boundary integral method," *Int. J. Numer. Methods Fluids* **48**(9), 1001–1021 (2005).